

1 **Air-Ice-Ocean Coupling During a Strong Mid-Winter Cyclone, Part 1: Observing
2 Coupled Dynamic Interactions Across Scales**

3 **D. M. Watkins¹, P. O. G. Persson², T. Stanton³, A. Solomon², J. K. Hutchings⁴, J. Haapala⁵,
4 G. Svensson⁶**

5 ¹Center for Fluid Mechanics, Brown University, Providence, RI, USA. ²Cooperative Institute for
6 Research in Environmental Sciences, University of Colorado, Boulder CO and NOAA/Physical
7 Sciences Laboratory, Boulder CO, USA. ³Moss Landing Marine Laboratories and Naval
8 Postgraduate School, CA, USA. ⁴College of Earth Ocean and Atmospheric Sciences, Oregon
9 State University, Corvallis, OR, USA. ⁵Finnish Meteorological Institute, Helsinki, Finland.

10 ⁶Stockholm University, Stockholm, Sweden

11 Corresponding author: Daniel Watkins (daniel_watkins@brown.edu)

12 **Key Points:**

- A ~~strong~~ cyclone crossed the Multidisciplinary drifting Observatory for the Study of the Arctic Climate (MOSAiC) in midwinter 2020
- Detailed, multi-platform observations enable characterization of coupled air-ice-ocean interactions during the passage of the ~~cyclone~~
- The development of a low-level atmospheric jet is a key factor in the spatially and temporally varying sea ice-ocean response [to the storm](#)

Deleted: pair of

Deleted: s

Deleted: se

Deleted: s

Deleted: to cyclones this cyclone[¶]

24 **Abstract**

25 Arctic cyclones are key drivers of sea ice and ocean variability. During the 2019-2020
26 Multidisciplinary drifting Observatory for the Study of Arctic Climate (MOSAiC) expedition,
27 joint observations of the coupled air-ice-ocean system were collected at multiple spatial scales.
28 Here, we present observations of a ~~strong mid-winter cyclone that impacted the MOSAiC site as~~
29 it drifted in the central Arctic pack ice. The sea ice dynamical response showed spatial structure
30 at the scale of the evolving and translating cyclonic wind field. Internal ice stress and ocean
31 stress play significant roles, resulting in timing offsets between the atmospheric forcing and the
32 ice response and post-cyclone inertial ringing in the ice and ocean. Ice motion in response to the
33 wind field then forces the upper ocean currents through frictional drag. The strongest impacts to
34 the sea ice and ocean from the passing cyclone occur as a result of the surface impacts of a
35 strong atmospheric low-level jet (LLJ) behind the trailing cold front and changing wind
36 directions between the warm-sector LLJ and post cold-frontal LLJ. Impacts of the cyclone are
37 prolonged through the coupled ice-ocean inertial response. Local impacts of the approximately
38 120 km wide LLJ occur over a 12 hour period or less and at scales of a kilometer to a few tens of
39 kilometers, meaning that these impacts occur at combined smaller spatial scales and faster time
40 scales than most satellite observations and coupled Earth system models can resolve.

41 **Plain Language Summary**

42 Arctic winter cyclones are an important part of the Arctic climate system. Yet, due to sparse
43 observations, processes of the coupled sea ice-ocean response to cyclones are not fully
44 understood. During the 2019-2020 Multidisciplinary drifting Observatory for the Study of Arctic
45 Climate (MOSAiC) expedition, observations of the atmosphere, sea ice, and ocean were
46 collected at a range of spatial scales. Here, we describe the atmospheric structure and coupled
47 ice-ocean response to a strong winter cyclone using data from surface weather stations, weather
48 balloons, radar, and a weather model. We then describe the sea ice motion using a large set of
49 GPS buoys and ice radar images. Finally, we examine the upper ocean currents and structure
50 using ocean buoy data. The most important part of the storm structure for the sea ice is the
51 development of an atmospheric low-level jet (LLJ), a narrow region of fast-moving air that
52 eventually circles around the storm. The sudden change in ice drift speed at the time that the LLJ
53 passes overhead enhances motion of the ice and ocean. Periodic currents in the ocean initiated by

Deleted: pair of

Deleted: s

Deleted: , with analytic emphasis on the second cyclone

Deleted: many

58 the sudden wind change of the LLJ continue for days following the passage of the storm,
 59 prolonging its effects.

60 **1 Introduction**

61 The physical environment in the Central Arctic consists of dynamically and thermodynamically
 62 coupled processes between the atmosphere, ice, and upper ocean (Brenner et al., 2023; Deser et
 63 al., 2015; Persson et al., 2017; Petty et al., 2016; Webster et al., 2019). Sea ice, and its
 64 accompanying snow cover, regulates the linkage between atmosphere and ocean through
 65 dynamics (lead opening and closing, evolving roughness of the air-ice and ice-ocean interfaces)
 66 and through thermodynamics as the ice and snow packs grow and melt (Maykut, 1982; Overland,
 67 1985; Persson, 2002, 2012; Pinto et al., 2003; Ruffieux et al., 1995; von Albedyll et al., 2022). In
 68 turn, the stability of the atmospheric and ocean boundary layers governs the evolution of
 69 turbulent eddies, affecting the magnitude of turbulent fluxes of heat and momentum (Andreas et
 70 al., 2010a, b; Grachev et al., 2007; Lüpkes et al., 2008; Lüpkes & Grynkiv, 2015; Taylor et al.,
 71 2018).

72 Arctic cyclones play a large role in this air-ice-ocean turbulent exchange. The large-scale
 73 pressure and mass fields of a cyclone produce strong cyclonic winds near the central low and in
 74 air-mass transport belts along fronts. Therefore, cyclone passage results in a pulse of momentum,
 75 heat, and moisture into the ice-ocean system. They represent major sources of poleward heat and
 76 moisture transport during Arctic winter (Fearon et al., 2021) and impact the surface energy
 77 budget, ice growth, snow accumulation, and even spring melt onset (Persson, 2012; Persson et
 78 al., 2017). Cyclone passage is often accompanied by strong sea ice deformation (Itkin et al.,
 79 2017; Lindsay, 2002; Oikonen et al., 2017) and enhanced ocean mixing (Meyer et al., 2017a,
 80 b). Cyclone impacts on sea ice depend on time of year, cyclone strength and evolutionary stage,
 81 location within the Arctic, location relative to the ice edge and coast, and the sea ice state (Aue et
 82 al., 2022).

83 The direct dynamic impacts of cyclones on the sea ice momentum equation, expressed in
 84 Equation 1 (e.g., Hibler, 1979; Hunke et al., 2015) are transferred through the atmospheric stress
 85 term, τ_a :

$$86 m \frac{D\mathbf{u}}{Dt} = -mf\mathbf{k} \times \mathbf{u} + \tau_a + \tau_o - mg \nabla H + \nabla \cdot \boldsymbol{\sigma} \quad (1)$$

87 The left side of (1) is the rate of change of the ice momentum with approximately constant mass
 88 m (snow and sea ice mass per unit area), where \mathbf{u} is the sea ice velocity. The sum of forces on
 89 the right-hand-side terms consists of the stresses on the ice due to the Coriolis force, where f is
 90 the Coriolis parameter, the atmosphere and ocean stress vectors $\boldsymbol{\tau}_a$ and $\boldsymbol{\tau}_o$, the effect of gravity
 91 down the slope of the ocean surface, and the divergence of the internal stress tensor. The last
 92 term represents energy loss due to friction between the floes and conversion of kinetic energy to
 93 potential energy, parameterized in terms of bulk and shear viscosities and ice strength. The
 94 coupled inertial response following the storm passage can prolong its dynamic effects (Haller et
 95 al., 2014).

96 The structure of the wind field within a cyclone imparts spatial gradients in the surface stresses,
 97 resulting in gradients of ice acceleration. As a result, the ~~dynamic sea ice response varies relative~~
 98 to the position of the low pressure center and the orientation of the storm track (e.g., Brümmer,
 99 2003; Haapala et al., 2005; Kriegsmann & Brümmer, 2014; Overland & Pease, 1982). Composite
 100 analysis based on reanalysis and satellite observations demonstrate that sea ice impacts have
 101 spatial structure, with dependence on distance from the storm center (Kriegsmann & Brümmer,
 102 2014) and position relative to the storm track (Clancy et al., 2022). However, estimates of
 103 cyclone structure and impacts based on composite analysis are sensitive to choices made in
 104 cyclone identification (Rae et al., 2017) and to the choice of reanalysis (Vessey et al., 2020).
 105 Differences in cyclone properties between reanalysis composites can arise from uncertainty in
 106 the physics of Arctic cyclones, differences in model implementation (including choice of
 107 parametrization schemes and model resolution), and the limited long-term in situ observations in
 108 the central Arctic, particularly joint observations of atmosphere, sea ice, and ocean.

109 Observations of the coupled air-ice-ocean system with the ability to resolve mesoscale cyclone
 110 features, including fronts, are extremely rare. ~~Thermodynamic~~ air-ice-ocean interactions for
 111 cyclones sampled during the Surface Heat and Energy Budget of the Arctic expedition (SHEBA;
 112 Persson, 2002; Uttal et al., 2002) have been analyzed in numerous studies (e.g., Lindsay, 2002;
 113 Persson, 2012; Persson et al., 2017; Richter-Menge et al., 2001; Shaw et al., 2009), providing
 114 case studies and seasonal and annual analysis. ~~However, air-ice-ocean momentum transfer~~
 115 ~~during cyclones is less well studied, especially with observations in all three media.~~ Both
 116 Lindsay (2002) and Richter-Menge et al. (2001) identify periods of enhanced mid-winter sea ice
 117 deformation that coincided with significant cyclone activity; however, the sea ice deformation

Deleted: thermodynamic and

Deleted: at least in part

Deleted:

Deleted: The

Deleted: through ice

Deleted:,

124 observations lack sufficient resolution to examine air-ice dynamic coupling in detail.

125 Measurements of sea ice motion and deformation show general patterns related to the storm
126 structure (Brümmer et al., 2008; Haller et al., 2014), with ice tending to diverge on average as
127 the cyclone passes. The location of the ice edge and the local history of deformation is an
128 important factor (Oikkonen et al., 2017).

129 The ocean response to wind forcing is strongly modulated by seasonal changes in ice thickness,
130 roughness, and concentration (Gallaher et al., 2016; McPhee, 2002, 2008; Meyer et al., 2017a;
131 Shaw et al., 2009; Stanton et al., 2012; Yang, 2004). Cyclones, and the strong gradients in winds
132 associated with them, result in changes in momentum transfer to the ocean that can excite inertial
133 oscillations in the ocean and ice (Brümmer & Hoeber, 1999; Hunkins, 1967), where the ice and
134 ocean move together in an inertial ringing ([Toole et al., 2010](#)). Though the presence of ice can
135 damp the ocean response (Brenner et al., 2023; Rainville & Woodgate, 2009), inertial

Deleted: The

Deleted: however

136 oscillations are observed in all seasons, including under consolidated winter ice pack (Martini et
137 al., 2014). This momentum transfer and the inertial motion enhances mixing in the upper ocean
138 and may also excite internal waves that enhance deeper mixing (McPhee & Kantha, 1989). High
139 wind speeds over sea ice have been observed to produce increased ocean friction velocity (Shaw
140 et al., 2009) and enhanced turbulent dissipation in the upper ocean (Meyer et al., 2017a). The
141 winter ice cover impedes momentum transfer from the wind to the ocean, reduces the inertial
142 response of the ocean, and likely sets the shallow winter mixed layer depth in parts of the Arctic
143 Ocean ([Toole et al., 2010](#)). Buoy observations of sea ice drift suggest that the inertial response of
144 the ice has been increasing (Gimbert et al., 2012; Yuan et al., 2022). It has been hypothesized
145 that an increase in sea ice inertial response may arise due to thinning of the ice pack (Gimbert et
146 al., 2012; Kwok et al., 2013) as well as increased cyclonic activity (Roberts et al., 2015).

147 To date, the full momentum transfer from wind, through ice to the ocean has not been observed
148 directly on the temporal and spatial scales that clearly define the roles of the spatial structure of a
149 cyclone for the associated ice and ocean response. To that end, we consider the detailed
150 observations of the coupled-air-ice-ocean system obtained during the Multidisciplinary drifting
151 Observatory for the Study of Arctic Climate (MOSAiC) expedition (Shupe et al., 2020; Shupe &
152 Rex, 2022). This study examines the relative roles of the atmospheric stress, ocean stress
153 (shearing between ice motion and upper-ocean currents), and the internal ice stress (via
154 consideration of sea ice deformation) in the momentum balance from MOSAiC observations

157 during the passage of an atmospheric cyclone, that traversed the study area between 30 January
 158 and 2 February, 2020. While there were numerous cyclones during the MOSAiC year (Rinke et
 159 al., 2021), this cyclone is of particular interest. It was intense, with high wind speeds and low
 160 minimum sea level pressure, and occurred at the beginning of a late winter–early spring period of
 161 unusually frequent cyclone activity with significant wind events (Rinke et al., 2021). The sea ice
 162 response to the February 1 cyclone included the fastest winter drift speeds in the MOSAiC drift
 163 and strong deformation of the ice pack. While some effects of this cyclone can be seen in
 164 meteorological time series covering the full MOSAiC year (e.g., López-García et al., 2022; Peng
 165 et al., 2023; and Shupe et al., 2022); and the cyclone drift track is shown in the supplement of
 166 (Rinke et al., 2021), no one has previously studied the air–ice–ocean dynamic interactions in
 167 detail for this, or any other, MOSAiC cyclone. As will be seen, this cyclone demonstrated
 168 common characteristics found by studies of synoptic events during the MOSAiC year, including
 169 synoptic modulation of boundary-layer stability characteristics (Jozef et al., 2023), moderate-to-
 170 intense snowfall (Matrosov et al., 2022), and continuous turbulence and deeper surface mixed-
 171 layer heights for stronger winds, especially when a low-level jet is present (Liu et al., 2023; Peng
 172 et al., 2023).

173 The proximity of the storm track to the MOSAiC observatory allowed detailed observations of
 174 the cyclone development and ice-ocean response. Furthermore, the cyclones occurred during the
 175 consolidated ice season in the high Arctic, when the internal ice stress term is expected to be an
 176 important part of the response.

177 The study highlights the atmospheric features producing the atmospheric stress characteristics,
 178 and the impacts of these stress terms on the sea ice and ocean motion. While the atmospheric
 179 stress is generally regarded as the primary forcing mechanism for ice motion, it is shown that
 180 both the internal ice stress and the ocean stress play significant roles in changing the typical air-
 181 ice interaction characteristics, including producing timing offsets between the atmospheric
 182 forcing and the ice response and producing post-cyclone inertial “ringing” responses in the ice
 183 and ocean. The MOSAiC observations and additional data are described in section 2. Sections 3-
 184 5 describe the observations of atmosphere, sea ice, and ocean, respectively. Discussion and
 185 conclusions follow in Section 6.

Deleted: two

Deleted: s

Deleted: these

Deleted: two

Deleted: s (especially the second cyclone) are

Deleted: They were

Deleted: T

Deleted: .

Deleted: such as

Deleted: moderate-to-intense snowfall (Matrosov et al., 2022).R

Deleted: Recent studies with relevance to MOSAiC cyclones have shown that the time period February through April had an unusual number of strong cyclones with significant wind events (Rinke et al., 2021), that consistent, radar-based precipitation measurements show about 110 mm of liquid-equivalent snowfall during October 2019 through May 2020, and that about half of that precipitation occurs with moderate or intense rates (Matrosov et al., 2022); and that the Arctic atmosphere tends to be strongly stable below ~1 km, with this stable layer sometimes elevated, and that there is some

Deleted: the

Deleted: ;

Deleted: .

Deleted: Atmospheric boundary-layer studies using MOSAiC data show that

Deleted: occur

214 **2 Data and methods**

215 The MOSAiC Central Observatory (CO) and its surrounding distributed network (DN) of
216 automated observational platforms and buoys were deployed in residual ice north of the Laptev
217 Sea in early October 2019, and drifted across the Central Arctic during the subsequent winter,
218 entering the Fram Strait in June 2020 (Krumpen et al., 2020). Maps showing the track of the
219 drifting station and more details of the atmospheric, ice, ocean and DN observations along this
220 drift track can be found in a series of MOSAiC overview ([Nicolaus et al., 2022; Rabe et al.,](#)
221 [2022, 2024; Shupe & Rex, 2022](#)) and domain-specific (e.g., Fer et al., 2022; Krumpen et al.,
222 2021; Peng et al., 2023; von Albedyll et al., 2022; Watkins et al., 2023) publications. Figure 1
223 shows a map of the relative positions of the CO and the DN sites on Jan 31, 2020, at which time
224 the CO was located at 87.5° N, 96.0° E (275 km from the North Pole). [Instruments used in the](#)
225 [study are described below, and summarized in Table S2.](#)

226 **2.1 Atmospheric observations**

227 Atmospheric observations used in this study were made at the CO (both on board the *R/V*
228 *Polarstern*, and at the “Met City” site located on the ice approximately 400 m from the ship), and
229 at the three “L” sites located 10–25 km from the ship (Figure 1). Key measurements from the
230 *R/V Polarstern* include the 6-hourly rawinsondes providing profiles of temperature, humidity,
231 and horizontal winds, and the vertically-pointing Ka-band radar providing profiles of radar
232 reflectivity and radial velocity. The 30-s radar data profiles were averaged to 10-min time
233 intervals for this study. A DOE/ARM scanning Ka-band radar provided volumes of radar
234 reflectivity and radial velocity approximately every 12 minutes, providing data for plane-parallel
235 indicator (PPI) displays characterizing clouds and precipitation. Post-field program reflectivity
236 calibrations were applied. Analyses of fronts and mesoscale features in the time-height cross
237 sections and horizontal displays relied on standard subjective analyses of thermodynamic (e.g.,
238 temperature, virtual potential temperature (θ_v), equivalent potential temperature (θ_e)), kinematic
239 (e.g., wind speed and direction), and radar reflectivity observations, not all of which are shown.
240 Changes in θ_e and wind direction and minima in SLP were key markers for determining frontal
241 boundaries. The Arctic inversion (AI) was defined as the height of the maximum temperature in
242 each sounding, and varied distinctly as synoptic conditions changed. Surface-based layers of
243 constant θ_v defined the surface mixed-layer (SML) depth for each sounding.

244 Sonic anemometers and basic meteorology sensors at Met City provided time series of
 245 temperature, humidity, winds, mean sea level pressure (SLP), and turbulence (including
 246 momentum flux) at 3 different levels (nominally 2, 6, and 10 m) and 4-component broadband
 247 radiative fluxes at ~2.5 m height. Atmospheric Surface Flux Stations (ASFS) located at the three
 248 L-sites provided measurements of temperature, humidity, pressure, and 4-component broadband
 249 radiative fluxes at ~2 m above the sea ice, and winds and turbulence (including momentum flux)
 250 at 3.8 m above the ice. The ASFS and Met City data used in this study are 10 minute average
 251 values. Unless otherwise stated, the Met City wind and turbulence data shown represents the 10
 252 m height while those at the ASFS represent the 3.8 m height.

253 Atmospheric stress was obtained through covariance calculations using the 10 Hz three-
 254 component (u, v, w) measurements from the sonic anemometers at Met City and the ASFS. First,
 255 the earth coordinate system is rotated into streamwise coordinates through a double rotation
 256 (Kaimal and Finnigan, 1994). The 10 minute values of friction velocity $u_a^* = (u'_s w')^{1/2}$ were
 257 then obtained from the integration of the cross-spectral density for a 13.65 minute window
 258 centered on the 10 minute period. Here, u'_s and w' are perturbation values of the streamwise and
 259 vertical wind speeds, respectively. The observed atmospheric stress is then calculated by $\tau_a =$
 260 $\rho_a u_a^{*2}$, where ρ_a is the atmospheric density. More detailed descriptions of the data processing,
 261 turbulence calculations and the atmospheric measurements on the *R/V Polarstern*, at Met City,
 262 and at the ASFS sites are provided by Shupe et al. (2022) and Cox et al. (2023).

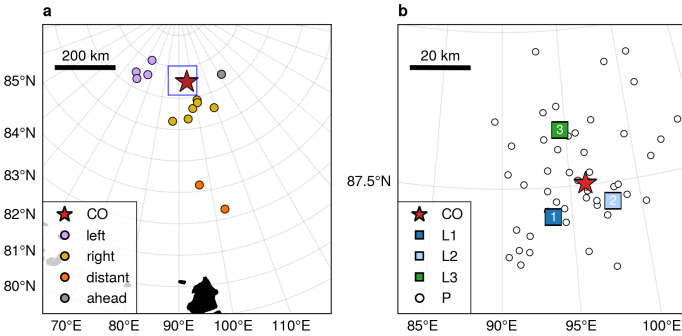
263 Time series of low-level atmospheric divergence are calculated from the winds at the three L-
 264 sites using the assumption that the winds vary linearly between the three sites. With this
 265 assumption, the area-averaged low-level atmospheric divergence div_a can be calculated using the
 266 area-normalized divergence theorem and by integrating the winds normal to the sides of the
 267 polygon such that

$$268 \quad \text{div}_a \approx \frac{1}{A} \left[\sum_{i=1}^{n_s} (\bar{u}_i dy_i - \bar{v}_i dx_i) \right] \quad (2)$$

269
 270 where $n_s = 3$ is the number of sides, \bar{u}_i, \bar{v}_i are the mean u and v wind components on side i , and
 271 (dx_i, dy_i) are the component lengths of each side i , and A is the area of the polygon. Because this

272 calculation is sensitive to errors in the installation and manual orientation of the sonic
 273 anemometers, we assume that the long-term mean divergence between ASFS sensor alignments
 274 is zero, and subtract this mean value from each value in the time series. For this case, the long-
 275 term mean divergence was $-1.1 \times 10^{-5} \text{ s}^{-1}$ calculated between 30 November, 2019, and 5
 276 February, 2020. Hence, magnitudes of div_a larger than $2 \times 10^{-5} \text{ s}^{-1}$ are likely significant.

277



278 **Figure 1.** MOSAiC domain and instrument locations on 1 February 2020 at 00:00 UTC. Shown
 279 are a) the extended DN and b) the DN, defined as buoys within 60 km of the CO. The extent of
 280 panel b is shown by the open blue square in panel a. The Central Observatory (red star labeled
 281 CO) and the 3 “L-sites” with the ASFS, SIMB and AOFB (squares, right hand panel) measure
 282 complete atmospheric, ice and upper-ocean parameters. The GPS ice buoys (circles) measure
 283 position, and their colors in panel a correspond to groups defined and highlighted in Figures 7
 284 and 9.

285 2.2 ERA5 atmospheric reanalysis

286 To obtain additional spatial atmospheric information, we supplement the atmospheric
 287 observations with 0.25° resolution data from the fifth-generation European Center for Medium-
 288 range Weather Forecasting reanalysis (ERA5; Hersbach et al., 2020) obtained from the
 289 Copernicus Data Store (Hersbach et al., 2023b, 2023a). Prior to analysis, the data was
 290 reprojected on a regular 25 km north polar stereographic grid with central longitude of 90° . The
 291 ERA5 reanalysis performs well relative to other reanalyses in the Arctic domain (Graham et al.,

292 2019a, b). ERA5 is known to have a surface warm bias in the Arctic (C. Wang et al., 2019; Yu et
 293 al., 2021), and ERA5 low-level jets are slightly weaker and slightly elevated (López-García et
 294 al., 2022). Here, we use ERA5 mean sea level pressure, 10-m winds, and 925 hPa temperature
 295 and humidity, and 950 hPa winds. ERA5 4D-var assimilation method uses a centered 12-h
 296 window, allowing impacts of observations to spread spatially and temporally. Rawinsonde and
 297 surface observations from the R/V Polarstern were assimilated by ERA5, while no measurements
 298 from the Met City tower or ASFSs were assimilated. In addition, ERA5 routinely assimilates
 299 SLP from drifting buoys (Hersbach et al., 2020). A subset of the MOSAiC drifting buoys
 300 measured sea level pressure and temperature, shared in near-real time via the World
 301 Meteorological Organization Global Telecommunication System. Thus it is likely that some
 302 spatial information from the buoys was incorporated into the reanalysis. Ice velocity from buoys
 303 is not assimilated. Hence, the ERA5 atmospheric structure should well represent the true
 304 atmospheric structure near the CO (as demonstrated for LLJs by López-García et al., 2022) and
 305 likely is the best available estimate of storm structure further away from the CO.

306 2.3 Sea ice observations

307 An array of drifting buoys, comprising the DN, track sea ice motion in the vicinity of the CO.
 308 Figure 1b shows the positions of the DN sites on February 1st, 2020 within 60 km of the central
 309 observatory. An additional 13 buoys comprise the “extended DN” (ExDN) and provide
 310 information on larger-scale ice motion (Figure 1a, colored circles). Each buoy reports positions
 311 via the Global Positioning System (GPS) with time resolution ranging from 10 minutes to 4
 312 hours; the majority of buoys sampled at least once every hour. We only use buoys with (a) time
 313 resolution of three hours or less and (b) at least 80% data coverage between 25 January and 5
 314 February 2020. Initial buoy processing is described in Bliss et al. (2023). In addition, anomalous
 315 points due to large random GPS errors were identified and removed by calculating the Z-score of
 316 the minimum of velocities estimated by forward and backward differences relative to a 3 day
 317 centered window. Observations were aligned to a 30 minute grid using natural cubic spline
 318 interpolation. During the study period, 64 buoys were operating, out of which 57 fulfill study
 319 criteria. These sites are referred to as position sites, or “P-sites”. An additional 11 sites
 320 (including the L-sites and the CO) contain multiple instruments. including sea ice mass balance
 321 buoys (SIMBs). We selected a reference buoy from each of these sites, preferring those with

Moved (insertion) [6]

Deleted: R

Deleted: MOSAiC central observatory

Deleted: as were surface measurements of temperature and air pressure from a few buoys from the MOSAiC DN

Deleted: (Hersbach et al., 2020)

Moved up [6]: ERA5 4D-var assimilation method uses a centered 12-h window, allowing impacts of observations to spread spatially and temporally.

330 higher sampling rate and data precision (Table S2). Choice of reference buoys is arbitrary in
 331 most cases, as the buoys at each site are closely situated.

Deleted: 1

332 The buoy trajectories provide information about the divergence, shear and vorticity of sea ice
 333 inside the DN. We calculate strain-rate components using a Green's Theorem method, following
 334 Hutchings et al., (2012, errata 2018). The area over which deformation is estimated can be varied
 335 depending on sites chosen to surround the region of interest. We consider deformation on a
 336 variety of scales including: the triangle with L-sites at its vertices, a set of 5 polygons with length
 337 scales of 15-30 km covering the DN, a polygon enclosing the full DN with length scale 57 km
 338 (Figure 10), and two polygons for the left and right sections of the ExDN (Figure 9). Hence, the
 339 DN Full array is an estimate of average deformation within the DN, while the smaller polygons
 340 in Figure 10 give an indication of the variability within the array.

341 2.4 Sea ice radar imaging

342 Local sea ice deformation observations were obtained from a ship radar-image digitizing system.
 343 The system was connected to the 9.4 GHz X-band radar mounted at the roof of the *R/V*
Polarstern (Hessner et al., 2019). Images of sea ice backscatter were collected with 8.3 m
 344 resolution every 2.5 seconds. We use a set of processed and georeferenced images (Krumpen et
 345 al., 2021a) downsampled to approximately 15 minute resolution. Images are centered at the *R/V*
Polarstern and extend radially to a distance of 3 nautical miles (approximately 5.4 km).

348 [Sea ice radar deformation time series have been provided by Uusinoka et al. \(2024\). The method](#)
 349 [uses an optical flow algorithm](#) track radar targets and estimate ice drift relative to the ship the
 350 [radar is mounted on](#). Images were recorded every 10 seconds, and averaged over 1 minute
 351 [intervals. Displacements were calculated with 10 minute intervals from the 1 minute mean](#)
 352 [images, from which the deformation is calculated.](#)

Deleted: The

Deleted: Their method is based on learning based

Deleted: is used to

Deleted: RADAR

Deleted: development

Deleted: RADAR images, r

Deleted: , were

Deleted: For this study, they provided a time series where

Deleted: d

Deleted: have been

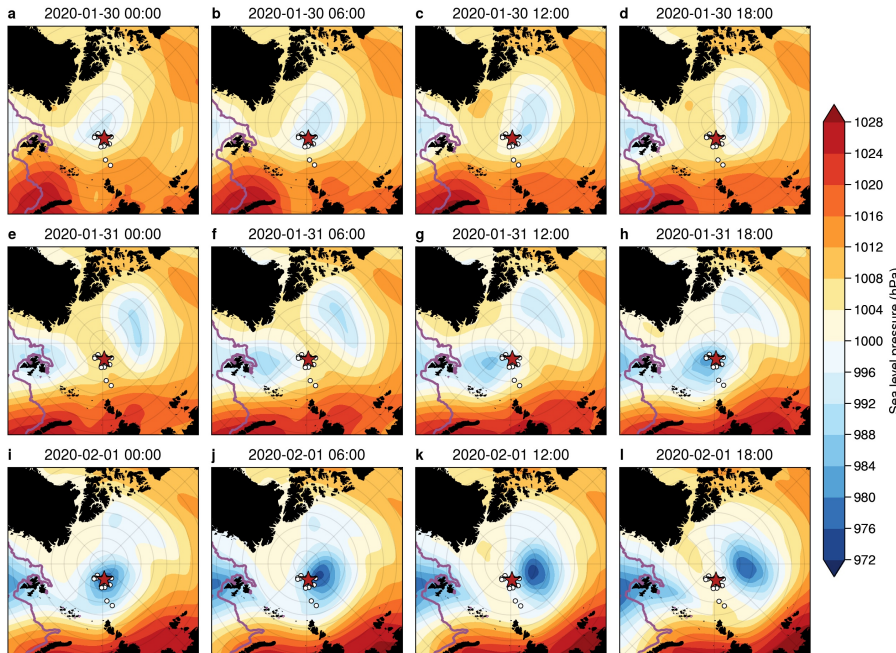
353

354 2.5 Upper-ocean turbulence and current measurements

355 Ocean timeseries observations were made from Autonomous Ocean Flux Buoys (AOFBs;
 356 Stanton et al., 2012) adjacent to the CO Met Tower and from the three L-sites. Each of these
 357 buoys supported a 5 m deep eddy-correlation turbulence sensor package providing direct heat,
 358 salt and momentum fluxes every 2 hours from 35-minute ensemble co-spectra of the 2 Hz

370 sampled 3-component velocity, temperature and conductivity timeseries. Ocean friction
371 velocities $u_o^* = (\langle u'w' \rangle^2 + \langle v'w' \rangle^2)^{\frac{1}{2}}$ from these co-spectra are used to infer the upper ocean
372 stress ($\rho_o u_o^{*2}$) at 5 m. A co-located Acoustic Doppler Current Profiler (ADCP) measured current
373 profiles from 6 m to 80 m depth sampling every 2.5 s and every 2 m in depth, and reporting 15-
374 minute ensembles with <1 cm s $^{-1}$ noise levels. Earth-referenced absolute current profiles were
375 calculated from the instrument-coordinate ADCP measurements by first rotating the component
376 profiles into true north coordinates using declination-corrected fluxgate compass measurements
377 in the ADCP and flux package, and, where possible, comparison with shipboard and ASFS GPS-
378 based heading observations. The AOFB / ice floe horizontal motion was then removed using the
379 AOFB GPS timeseries to form absolute u/v vector current profiles.

380 In this study, we use ocean measurements from the CO site adjacent to the main Met City tower.
381 Water density profiles were calculated from the intermittent ship's [Conductivity, Temperature,](#)
382 [Depth \(CTD\)](#) and microstructure profiling program at the CO. Difficult operating conditions
383 during this period of very high winds limited CTD sampling at the CO to as little as once per
384 day. Seasonal mixed layer depths are estimated from the depth in each profile where there is a
385 0.2 kg m $^{-3}$ potential density increase from the 8 m near-surface values. These sparse-in-time
386 mixed layer depths are linearly interpolated in time and smoothed with a 12-hr period running
387 average filter to estimate the depth of the top of the strong halocline observed across much of the
388 Arctic. A much more sensitive density threshold of 0.01 kg m $^{-3}$ is used as an indicator of the base
389 of the active surface boundary layer in the analysis in section 5.

390 **3 Atmospheric structure and evolution**391 **3.1 Synoptic evolution**

392

393 **Figure 2.** Sequence of ERA5 mean sea-level pressure (SLP) analyses at 6-hour intervals from 30
 394 January 00:00 UTC to 1 February 18:00 UTC. The red star indicates the location of the CO, and
 395 the white circles show the buoys in the DN and ExDN. The position of the ice edge from the
 396 daily NSIDC 12.5 km AMSR2 sea ice concentration (SIC), defined as the 15% SIC isopleth, is
 397 indicated with a purple line.

398

399 Two cyclones crossed the MOSAiC domain in short succession between January 29th and
 400 February 1st, 2020 (Figure 2). The first cyclone (C_1) developed along the NE coast of Greenland
 401 on 29 January, strengthening slightly as it moved northward over the North Pole (Figure 2a-c).
 402 Soundings at the *R/V Polarstern* suggest that a warm front/cold front couplet developed with the

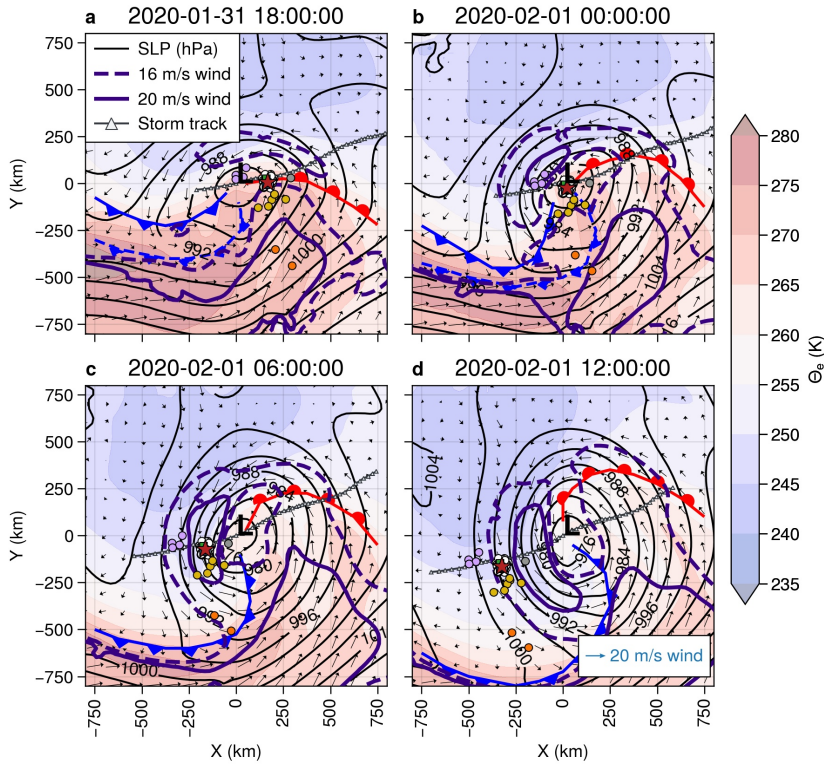
Deleted: (discussed in Section 3.2)

403 system and that the warm sector passed over the MOSAiC domain. As this first cyclone was
404 passing the MOSAiC domain, a second cyclone (C_2) developed along the west coast of Svalbard
405 on 30 January and strengthened along Svalbard's north coastline as it moved northward (Figure
406 2c). C_2 is the primary cyclone of interest for this study. While C_1 only deepened by about 7 hPa
407 along its track, C_2 deepened by nearly 20 hPa, becoming one of the deepest cyclones to pass over
408 the MOSAiC domain during the year (Figure 2i). The observed SLP minimum (974 hPa) in the
409 MOSAiC domain during C_2 was 4 hPa lower than the minimum central pressure in the ERA5
410 fields, indicating that the observed cyclone was slightly stronger than in ERA5. A warm
411 front/cold front couplet also developed with this system, both of which passed over the MOSAiC
412 observatory.

413 3.2 Key mesoscale structures

414 Figure 3 shows an atmospheric frontal analysis of C_2 based on the 6-hourly ERA5 mean sea-level
415 pressure, 10 m wind vectors, 925 hPa equivalent potential temperature (θ_e), and 950 hPa wind
416 speed centered at the location of the SLP minimum. In this and following figures, references to
417 cardinal directions are relative to the CO. The polar stereographic maps are oriented so that north
418 from the CO is in the positive y direction and east is in the positive x direction; note that the
419 North Pole is 267 km north of the CO, so the direction of true north will vary substantially
420 throughout the figure. The storm deepened by 8 hPa during the 18 hours shown and has clear
421 spatial structure, with northward warm-air advection in the warm sector primarily to the right of
422 the storm track ahead of the low center and southward cold-air advection in the cold sector
423 primarily to the left of the storm track and behind the low center. The surface warm front passes
424 over the CO (red star) on 31 January between 14 UTC and 16 UTC (Figure 3a), while a cold
425 front aloft passes over the CO on 31 January near 23 UTC and a surface cold front passes over
426 the CO near 02 UTC. The surface low passes very close to the CO but just to its west and north,
427 such that the CO is initially in the warm sector air before being affected by the trailing surface
428 cold front. Strong low-level wind speeds indicating a low-level jet (LLJ) initially occur in the
429 warm sector between the warm front and the cold front aloft. By 1 February 00 UTC (Figure 3b),
430 a LLJ (indicated here by the 16 m s⁻¹ isotach at 950 hPa) encircles the surface low and remains as
431 a nearly axisymmetric annulus through the rest of the time period as the system occludes with
432 bands of warm and cold air wrapping around the low center (Figure 3c,d). Figure 2 suggests that
433 C_2 was more axisymmetric (circular) than C_1 . While C_2 is quasi-axisymmetric initially and

435 becomes even more axisymmetric as it strengthens, C_1 starts out more elongated and becomes
 436 even more so with time. C_1 appears eventually to be absorbed into C_2 . We hypothesize that the
 437 symmetry of the storm is an important factor in the development of the axisymmetric mesoscale
 438 LLJ annulus.



439

440 **Figure 3.** ERA5 reanalyses centered on the SLP minimum for cyclone C_2 . Shown are SLP (hPa;
 441 black isopleths), 925 hPa equivalent potential temperature θ_e (K; colors), 10 m wind vectors, and
 442 select 950 hPa isotachs (16 and 20 m s⁻¹; green). Every fourth wind vector is plotted for clarity;
 443 vector length is proportional to wind magnitude. The heavy red and blue lines show the positions
 444 of the warm and cold fronts, respectively. Dashed front lines indicate thermal features aloft,
 445 while the solid lines depict fronts at the surface. The light gray line shows the track of the low

446 center within the domain, while the colored circles show buoy positions. Colors for DN and
 447 ExDN sites are as in Figure 1.

Deleted:

448 Utilizing the near-surface observations at the three ASFS sites and at the CO, rough
 449 observational surface analyses are possible on the ~50 km scale of the DN. Figure 4 shows
 450 isotherm analyses centered on the CO between 31 January 14:05 UTC, just prior to the passage
 451 of the surface warm front, and 1 February 06:41 UTC, nearly 5 hours after the passage of the
 452 surface cold front. These are overlaid on low-elevation radar-reflectivity PPI scans to provide an
 453 indication of the spatial distribution and structure of the clouds (<~0 dBZ) and precipitation (>
 454 ~0 dBZ).

455 Moderate ($5\text{-}10 \text{ m s}^{-1}$) southeasterly surface winds were present throughout the domain as the air
 456 temperatures warmed with the approaching surface warm front (Figure 4b). Winds were initially
 457 moderate from the SSW but decreased in magnitude as the low-pressure center neared the CO,
 458 particularly after the cold-front aloft passed overhead. The more cellular nature of the clouds
 459 and precipitation after the cold front aloft passed can be seen in comparing Figure 4c and 4d,
 460 validating the analysis of the upper-level cold front in Figure 3a and 3b. The trailing surface
 461 cold front entered the DN from the NW, marked by a sudden wind shift to the N and a trailing,
 462 very strong temperature gradient (Figure 4e-g). The cold front took about 1.5 h to traverse the L-
 463 site triangle. The northerly winds increased throughout this frontal zone, reaching near-surface
 464 speeds of $12\text{-}15 \text{ m s}^{-1}$ as the LLJ behind the front passed overhead (Figure 4h-i). High wind
 465 speeds combined with strong cold-air advection shown in these last two panels leads to strong
 466 mixing near the surface, producing what appears to be horizontal roll vortices in the atmospheric
 467 boundary layer (suggested by the linear, along-wind, cloud and precipitation features).

Deleted: Within the warm sector, temperatures gradually warmed to -11 °C.

468 Horizontal roll vortices are an efficient mechanism for vertical mixing in the atmospheric
 469 boundary layer (Etling & Brown, 1993; LeMone, 1973), so their presence indicates that the
 470 momentum transfer from the LLJ down to the surface just behind the cold front is particularly
 471 effective. Figure 4 suggests that roll vortices produce the deepening of the surface mixed layer,
 472 behind the cold front (Figure 5a) and greatly enhance the surface atmospheric stress. Figure 4
 473 shows that the CO observations were made through the warm front, the warm sector, and the
 474 cold front, and confirms that the cyclone center passed to the north of the CO.

Deleted: .

Deleted: Air temperatures dropped to between -27 °C and -30 °C. ...

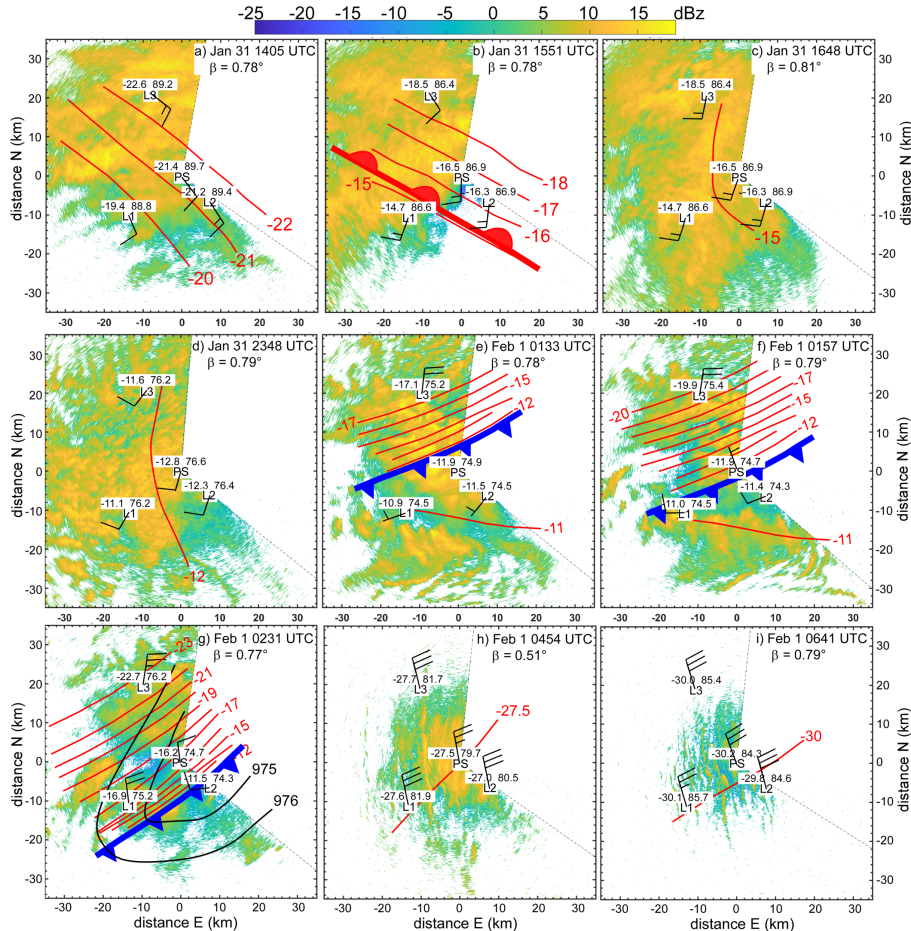
Deleted: effective

Deleted: .

Deleted: also confirms

Deleted: is the only purely observational analysis we have

Deleted: ing



486

487 **Figure 4.** Near-surface meteorological observations of air temperature ($^{\circ}\text{C}$, [text to the upper left of station labels](#)), SLP (hPa [minus 900](#), [text to the upper right of station labels](#)), and wind barbs
 488 from the three L-site ASFSs (3.8 m) and at Met City (6 m). [The panels emphasize](#) the warm-
 489 frontal (heavy red, lobed line) passage on 31 January (a-b), cold frontal (heavy blue toothed line)
 490 passage on 1 February (e-g), and [conditions](#) in the post-cold-frontal sector (h-i). [Red lines show](#)
 491 [manual isotherm analysis](#) with 1°C isotherm interval. Panels with only one isotherm represent
 492 times when the spatial temperature difference between sites is less than 1°C . [Reliable isobar](#)
 493

Deleted: blue**Deleted:** blue**Deleted:** downwelling longwave radiation (W/m²)**Deleted:** during**Deleted:** M**Deleted:** of**Deleted:** air temperature is shown in red lines

501 analysis could only be done for panel g (hPa; black lines). The background shows PPIs of the
 502 given low-elevation (β) scanning Ka-band radar reflectivity (color, dBZ). Thin, dashed, black
 503 radii bracket the region not scanned by the radar. North is upwards for each panel.

504 A time-height section of serial rawinsonde data and near-surface time series of various
 505 parameters (Figure 5) confirm the features passing over the MOSAiC domain discussed above.
 506 The passage of the first cyclone (C_1) and its associated narrow warm-sector are clearly seen, with
 507 the brief but distinct warm air peak in the warm sector, and the cooling and veering of the
 508 surface wind with the passage of the cold front. A LLJ is present at approximately 250 m above
 509 the surface near the time of the warm-frontal passage. The second cyclone (C_2) is deeper with a
 510 broader warm sector over the CO. The air warms only slightly in the warm sector between the
 511 warm front and the cold front, but the thermal wind effect from this thermal gradient, with the
 512 warmest air closest to the cold front, is a likely cause for the observed LLJ within the warm
 513 sector at 250-300 m height. The rawinsondes show the warm-sector LLJ wind speed maximum
 514 near 15 m s⁻¹ just above the surface mixed layer (SML), with associated near-surface wind
 515 speeds of 7-8 m s⁻¹ (Figure 5a, d; Figure 4c).

516 The passage of the cold front with C_2 near 02 UTC on 1 February marks the time of the lowest
 517 observed central pressure (974 hPa), a very sharp drop in surface temperature, a minimum in
 518 surface winds, and a rapid change in surface wind direction (Figure 5b-e; Figure 4e-g). A
 519 second LLJ is observed at ~350-400 m height just behind the cold front with a core speed of 21-
 520 22 m s⁻¹ and with temporarily deeper SML as indicated by the constant θ_v with height. Just after
 521 the cold-frontal passage, the near-surface wind speed increases with the arrival of the LLJ above,
 522 reaching speeds of 14-16 m s⁻¹ across the four observational sites between 04 and 06 UTC on 1
 523 February (see also Figure 4h-i). The timing differences in the wind direction shifts, wind speed
 524 increases, and temperature decreases between sites (Figure 5d-e) represent the progression of the
 525 cold front across the DN from the northwest. Stability differences in the sub-jet layers may
 526 cause the higher surface wind speed relative to its core strength for this second post-cold-frontal
 527 LLJ when compared to the warm-sector LLJ. A peak in the observed covariance surface stress
 528 (τ_a) at Met City (Figure 5f) occurs just after the cold frontal passage, and is coincident with the
 529 deepening of the SML just below the LLJ (Figure 5a) and the appearance of the likely horizontal
 530 roll vortices (Figure 4h-i). It is unclear whether enhanced turbulence caused by the LLJ or the

Deleted: Isobar analysis is depicted with black lines in panel g. ...

Deleted: Range rings (black dashed lines) are shown at 5, 15, 25, 35, and 45 km distances, and are labeled with the radar-beam height (m) above the local surface.

Deleted: he t

Deleted:

Deleted: a very sharp drop in surface temperature (-11°C to -38°C in only 12 h),

540 roll vortices have deepened the SML, or if the deeper SML has weakened the near-surface winds
 541 thereby producing a LLJ just above the SML. The ASFS surface stress measurements at L1 and
 542 L2 are nearly identical to those at MC, except for the expected slight differences in timing (see
 543 Figure S1). Site L3 also showed the large stress increase just after the cold frontal passage. The
 544 otherwise slightly different stress time series at L3 was likely impacted by the significant ice
 545 dynamics occurring at that site with this cyclone. Indeed, the L3 ASFS was flipped on its side by
 546 a growing ice ridge early on February 4. All of these features at the various sites indicate
 547 significant, efficient, vertical momentum transport just after the cold-frontal passage.

548 The presence of the LLJ behind the cold front is likely due to the LLJ being quasi-axisymmetric
 549 around C₂. This “wrap-around” LLJ may be an extension of the LLJ observed in the warm sector
 550 as this warm air wraps around the strong but compact cyclone center, as seen in Figure 3a-d.
 551 Note the temperature within this wrap-around LLJ decreased, and is at a slightly higher altitude,
 552 consistent with some lifting as the LLJ wrapped itself around the cyclone center. This is
 553 consistent with the concepts of frontal fracturing and warm and cold conveyor belts for
 554 occluding midlatitude cyclones (Carlson, 1980; Shapiro & Keyser, 1990). The weak decrease in
 555 wind speed above the LLJ core is likely due to the implied horizontal thermal gradient and
 556 thermal wind over a ~100 m deep layer at the core of this second LLJ. Fully studying the details
 557 of the LLJ dynamics with this Arctic cyclone is beyond the scope of this paper.

558 We suggest that the presence of two LLJs in fairly rapid succession, possibly parts of a wrap-
 559 around LLJ within a rapidly moving cyclone, produces strong, rapid surface wind speed and
 560 wind direction changes as it translates across the MOSAiC domain. Moderate southerly winds in
 561 the warm sector rapidly change to very strong northerly winds within a few hours behind the
 562 cold front. We suggest that this is a key forcing for the significant ice motion, ice deformation
 563 and upper-ocean current changes observed during the passage of the cyclone on 1 February. The
 564 strength of the LLJ behind the cold front and the enhanced vertical mixing also contributes to the
 565 ice impact being particularly linked to that feature in time. Such a double LLJ (wrap-around LLJ)
 566 was also observed in other MOSAiC cyclones with significant ice deformation (e.g., Persson et
 567 al., 2023), with most of the ice deformation occurring when the wind transitions from strong
 568 southwesterly winds to strong northerly winds. Details of the ice response to this 1 February
 569 cyclone are given in Section 4.

Deleted: All of these features indicate significant, efficient, vertical momentum transport at this time.

Deleted: is likely

Deleted: that

Deleted: the

Deleted: has

Deleted: that

Deleted: cold sector LLJ

Deleted: it

Deleted: than the LLJ in the warm sector

Deleted: has

Deleted: occluding

Deleted: .

Deleted: There is likely a

Deleted: contribution

Deleted: infer

Deleted: As will be shown

Deleted: ,

Deleted: T

Deleted: the

Deleted: C₂.

Deleted: Feb 1

Deleted: .

593 Low-level atmospheric divergence is one way to quantify these wind transitions. Indeed, we
594 observe significant atmospheric convergence with the passage of the warm and cold fronts of the
595 1 February cyclone, with the strongest convergence ($\sim 30 \times 10^{-5} \text{ s}^{-1}$) occurring with the cold-
596 frontal passage (Figure 5g). Ice convergence and shear also peak across the DN at this time,
597 which will be discussed in more detail in the next section. There is no appreciable ice
598 divergence/convergence within the L-site triangle associated with the warm frontal passage,
599 though there is significant shearing of the ice (Figure 5g). Note that another substantial wind
600 transition event with atmospheric divergence/convergence (3 February 08 UTC) shows only
601 weak ice deformation, while large ice deformation near 30 January 11 UTC occurs about 4 h
602 after the wind changes. Ice deformation events are only sometimes concurrent with wind
603 transitions and atmospheric divergence, and can have multiple local and nonlocal causes.

Deleted: cyclone C₂

Deleted:

Deleted: ing

Deleted: show

Deleted: s

Deleted:

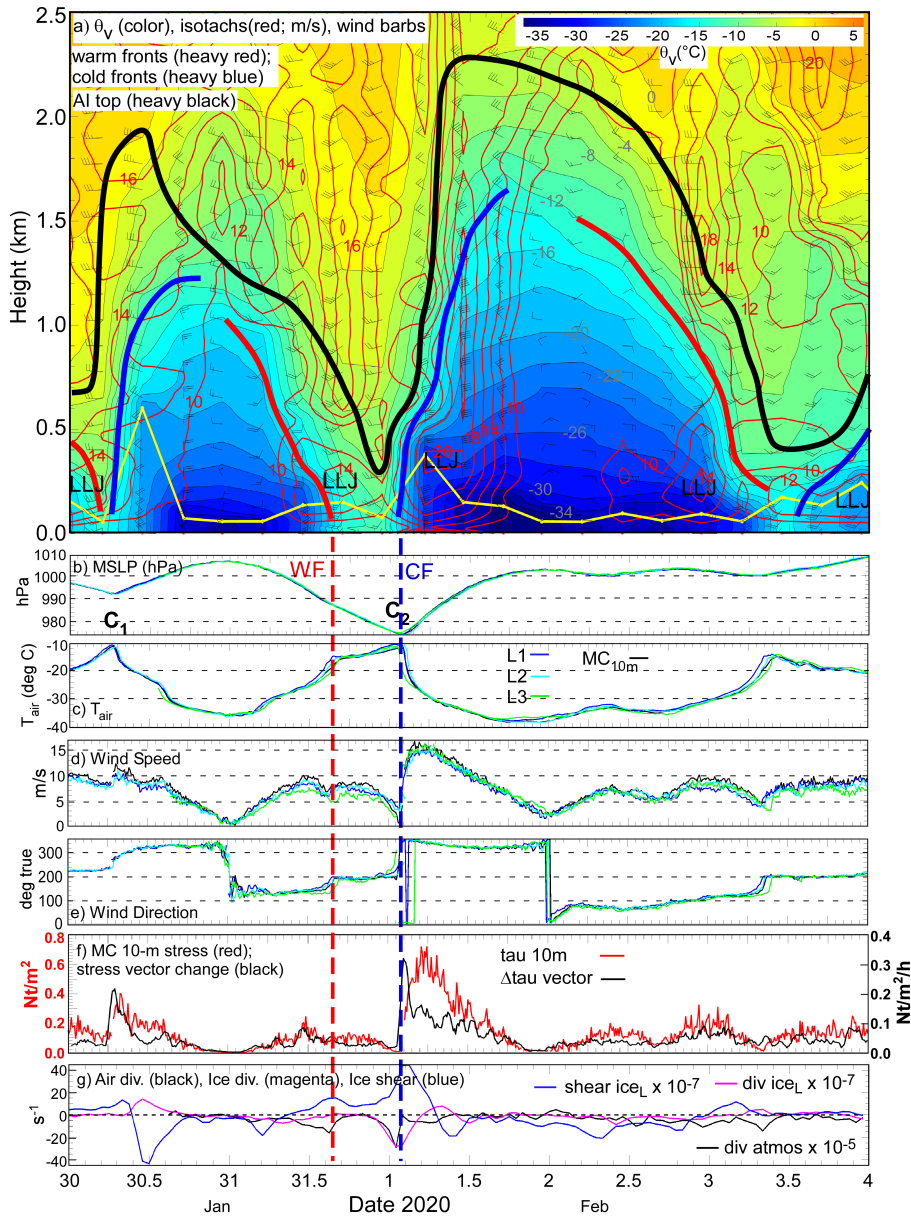
Deleted: significant

Deleted: without significant wind changes and

Deleted: such

Deleted: Hence, i

Deleted: Note that other substantial wind transition events
also show some atmospheric divergence/convergence and
some ice deformation (e.g., near 08 UTC on 3 February, also
associated with a LLJ). Nevertheless, ice deformation events
can have multiple local and nonlocal causes, and therefore
are only sometimes associated with local atmospheric
divergence....



622 **Figure 5.** a) Time-height section of virtual potential temperature (θ_v colors; °C, gray labels),
 623 isotachs (red), and select wind barbs from serial rawinsondes at the *R/V Polarstern*. Heavy (red,
 624 blue, black) lines mark warm and cold fronts and the top of the Arctic inversion (base of the free
 625 troposphere), respectively. The thin yellow line marks the top of the surface mixed-layer. Low-
 626 level jets (LLJ) are also marked. Rawinsondes were launched every 6 hours, launch times
 627 indicated by the origin of the wind barbs. Lower 6 panels: Time-series from the Met City tower
 628 and the ASFSs of b) MSLP; c) T_a ; d) 10 m (Met City) and 3.8 m wind speed; e) 10 m and 3.8 m
 629 wind direction; f) 10-m atmospheric stress (red), stress vector change (black) at [Met City](#); and g)
 630 3.8 m atmospheric divergence (red), ice divergence (blue), and ice shear (green). The vertical
 631 dashed lines show the times when the warm (red) and cold (blue) fronts with the second cyclone
 632 pass over. C₁ and C₂ mark the minima in MSLP with first and second cyclone, respectively.

Deleted: C

633 4 Sea ice dynamics

634 In late January and early February midwinter pack ice conditions were present. Ice thickness
 635 measured at thirteen mass balance stations (Nicolaus et al., 2022; Perovich et al., 2023) ranged
 636 from 1 m to 2 m. Increases in the mass of the snow and sea ice from 30 January 00 UTC to 02
 637 February 00 UTC due to bottom growth (2–4 cm) and snowfall (1.1 cm liquid water equivalent,
 638 Matrosov et al., 2022) are minor relative to the ice thickness during this event, so the ice mass in
 639 eq. 1 can be considered to be constant. For events with much thinner ice, mass changes due to
 640 snowfall and bottom growth may need to be considered when analyzing the ice dynamics. In
 641 this section we consider first the relationships between wind and ice velocities, and then the sea
 642 ice deformation, noting in particular the role of the spatial scales of the atmospheric forcing
 643 relative to the ice motion and deformation.

Deleted: M

Deleted: during the study period

Deleted: es

Formatted: Text

Deleted: ing

Deleted: is

Deleted: During the two cyclones thermodynamic changes to the ice pack, and the impact of snow on the surface are small. There may be changes in the surface roughness due to lead opening and ridging, which we do not sufficiently detailed observations to resolve.

Deleted: W

644 4.1 Atmosphere-ice interaction

645 Large scale sea ice motion in the Central Arctic is known to be strongly correlated with winds at
 646 large scales (1000 km) and at time scales comparable to synoptic systems in the atmosphere
 647 (days to weeks) (McNutt & Overland, 2003; Thorndike & Colony, 1982). At shorter time scales,
 648 sea ice is known to respond rapidly to strong shifts in wind speed (such as during cyclone
 649 passage), though the local ice velocity may not be coherent with local wind speed due to internal
 650 ice stresses and other effects (Hutchings et al., 2011; Itkin et al., 2017; Lei et al., 2020; Overland

et al., 1995). The MOSAiC measurements show sea ice motion broadly coherent with the time-varying wind forcing, with the ice moving to the right of the wind (Figure 6) in accordance to the right-hand rule first noted in the *Fram* expedition results (Nansen, 1902). Note that the wind velocity in ERA5 is in good agreement with the observed winds (dark and light blue arrows in Figure 6a-d). The drift speed ratio (α , the ratio between the local drift and wind speeds) and net turning angle (θ , the difference between the local wind and drift directions) are empirical measures of the relationship between the ice drift and the wind speed. In steady state free drift, θ is a function of the boundary layer structure and the ice surface roughness, and α is a function of the air-ice and ice-ocean drag coefficients and the densities of each medium (Leppäranta, 2011). During the study period, average values of α and θ are 0.021 and 35°, respectively, consistent with previous studies (Leppäranta, 2007; Schweiger & Zhang, 2015; Womack et al., 2022). However, both θ and α vary significantly over time (Figure 6e, f). Drift speed ratios are low in the warm sectors of both cyclones, while they increase after the arrival of the cold fronts, remaining high after the passage of the 1 February cold front. Increases in α following cyclone passage has been observed previously (e.g., Itkin et al., 2017). In the absence of a step change in the strength of the ocean current, the observed increased drift speed ratio suggests that a larger fraction of atmospheric momentum is being converted into ice motion rather than adding to the internal ice stresses. The turning angle in the warm sector is slightly larger than the mean for the first cyclone but below the mean for the 1 February case. Following this second cyclone, we note apparent oscillation in both θ and α , near the inertial frequency (~12 hours), suggesting the possibility of inertial oscillations following the storm.

Deleted: Sea ice motion during the passage of the cyclones is

Moved (insertion) [1]

Deleted: T

Moved (insertion) [2]

Deleted: For the period shown in Figure 6e-f,

Field Code Changed

Moved up [1]: Note that the wind velocity in ERA5 is in good agreement with the observed winds (dark and light blue arrows in Figure 6a-d).

Moved up [2]: For the period shown in Figure 6e-f, average values of α and θ are 0.021 and 35, respectively, consistent with previous studies (Leppäranta, 2007; Schweiger & Zhang, 2015; Womack et al., 2022).

Deleted: The drift speed ratio and turning angle are empirical measures of the relationship between the ice drift and the wind speed. In steady state free drift, θ is a function of the boundary layer structure and the ice surface roughness, and α is a function of the air-ice and ice-ocean drag coefficients and the densities of each medium.

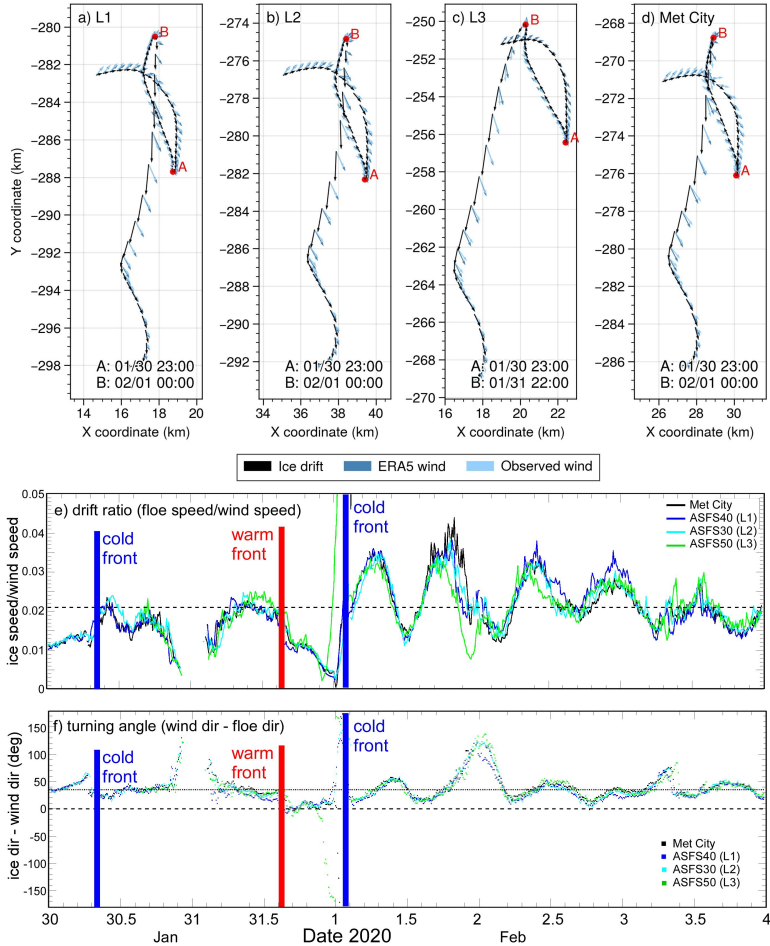
Moved (insertion) [3]

Deleted: .

Moved up [3]: Increases in α following cyclone passage has been observed previously (e.g., Itkin et al., 2017).

Deleted: . The turning angle in the warm sector is slightly larger than the mean for C_1 , but below the mean for C_2 . Drift speed ratio remains high after the cold front on 1 February, which suggests that a larger fraction of atmospheric momentum is being converted into ice motion rather than adding to the internal ice stresses.

Deleted: The drift speed ratio following the second cyclone passage oscillates



712

713 Figure 6. Top a-d: Trajectories of sites L1, L2, L3, and Met City at hourly resolution from 30
 714 January 00:00 UTC on 02 February 00:00 UTC. Black arrows indicate the ice drift direction,
 715 light blue the observed wind direction, and dark blue the estimated wind from the ERA5
 716 reanalysis. Arrow length is proportional to speed; wind speeds are scaled to 2% for comparison
 717 with the drift speed. Bottom: (e) Drift speed ratio (ice speed divided by wind speed) and (f)
 718 empirical turning angle (difference between wind direction and ice drift direction) derived from
 719 local 10-min wind and ice drift observations at sites L1, L2, L3, and Met City.

720

721 Drift trajectories of the three L-sites and the CO [demonstrate gradual and abrupt ice motion](#)
 722 [following local changes in the advected wind field](#) (Figure 6a-d). At all four sites, the ice drift
 723 arcs to the right and slows as the [first cyclone](#) moves away from the MOSAiC site. During the
 724 passage of the pressure ridge between cyclones, the wind direction abruptly reverses (Figure 5e;
 725 Figure 6a-d). This reversal occurs at 23 UTC on 30 January at all sites, marked by the red letter
 726 A. As SLP decreases and [the 1 February cyclone](#) approaches the CO, the ice drifts northward due
 727 to southerly winds until slowing to a halt and again reversing direction. The cusp in the trajectory
 728 marking the reversal is indicated by the letter B. Notably, this reversal precedes a rapid
 729 acceleration, and occurs at different times at each site: first at 22:30 UTC on 31 January at L3,
 730 next at 0 UTC on 1 February at sites L1 and at the CO (Met City), and last at 0:30 UTC on 1
 731 February at L2. These times are all about 2 h prior to the passage of the cold front and the large
 732 change in wind direction at each site ([see also times in Figure 4](#)). [A broader view is seen through](#)
 733 [examination of cusps in DN buoy trajectories](#), identified by local minima in drift speed. Cusp
 734 timestamps display a west-east gradient spanning a 3-hour period consistent with ~ 25 km/h (~ 7
 735 m s $^{-1}$) cyclone propagation speed (Figure 7b), with some deviations likely due to propagating
 736 internal ice stresses from nonlocal forcing. Further from the storm center, 48-hour drift
 737 trajectories show clockwise motion to the right of the storm (Figure 7c, d) and counter-clockwise
 738 motion to the left (Figure 7a), with the sharpness of the turn increasing nearer the storm center
 739 due to the smaller radii of the quasi-annular wind around the low center.

740

Deleted: generally illustrate the expected right hand turning rule ($\theta > 0$) first noted by Nansen (1902)

Deleted: cyclone C₁

Deleted: C₁ and C₂,

Deleted: C₂

Deleted: Also, compare times to

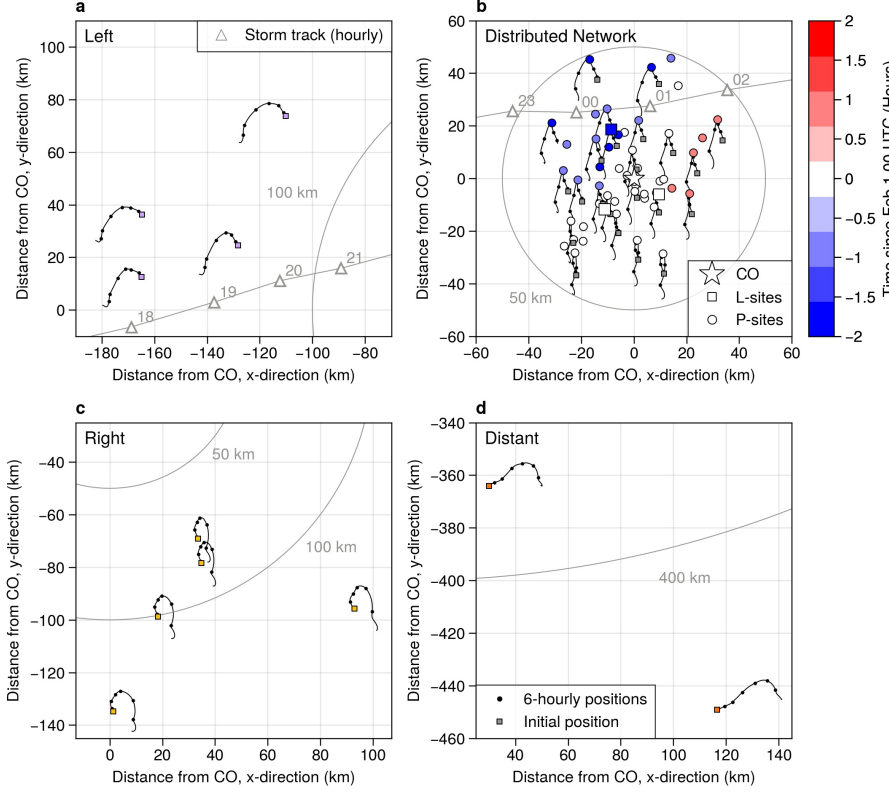
Deleted: .

Deleted: C

Deleted: are

Deleted: That is, it appears as if the 2 h difference in wind and ice drift direction changes and the deviations in the propagation of the ice drift reversals may be due to internal ice stresses caused by non-local wind forcing behind the cold front. ...

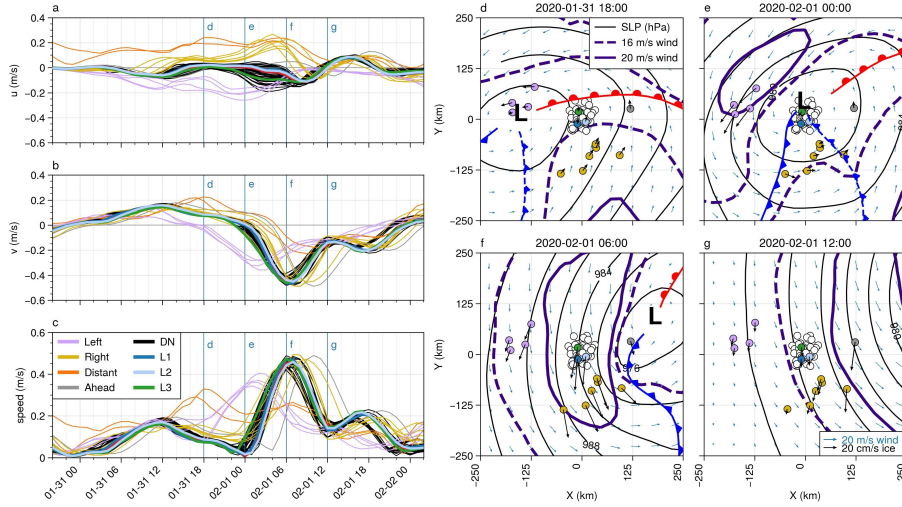
Deleted: ¶



756

757 **Figure 7.** Buoy trajectories from 31 January 00:00 UTC to 2 February 00:00 UTC. Small
 758 squares indicate the beginning of the time series. Black lines show the 30-min resolution drift
 759 tracks, and black circles show the position every 6 hours. Distance from the CO is indicated with
 760 the axis units and radii at 50 km, 100 km, and 350 km. In panel b, the time of the drift speed
 761 minimum relative to 1 February 00:00 UTC is indicated with color. Trajectories of a subset of
 762 DN buoys are shown for clarity. L-sites are marked with large squares, while the CO is marked
 763 by a star. In panels a and b, the position of the sea level pressure low from the ERA5 reanalysis
 764 is marked at hourly intervals with triangles and labeled with the corresponding hour of day.

765



766

767 **Figure 8.** Left: Buoy velocity components (a, b) and magnitude (c) for the period from 30
 768 January 20:00 UTC to 2 February 02:00 UTC. The top and middle panels show the u and v
 769 velocity components relative to the north polar stereographic projection, thus corresponding to
 770 the x and y axis, respectively, in the panels on the right. For the period shown here, the positive y
 771 direction is approximately northward. Right: Snapshots of buoy motion (thick black arrows)
 772 superimposed on the ERA5 sea level pressure isobars (black contours, 4 hPa spacing), near-
 773 surface (10 m) wind fields (blue arrows), and 16 and 20 m s⁻¹ isotachs of the 950 hPa winds
 774 (green contours) at times corresponding to vertical lines in the velocity time series to the left.
 775 The position of the SLP minimum is marked with “L”. The cold front is marked in blue and the
 776 warm front is marked in red. Solid fronts are surface level and dashed are elevated.

777 The clearest sign of the storm’s impact on the ice velocity is through the effect of the LLJ as it
 778 develops and moves across the MOSAiC array. High ice drift speeds indicate efficient downward
 779 mixing of momentum through the atmospheric boundary layer. Soundings and ship surface
 780 meteorological data were assimilated by ERA5 (Rinke et al., 2021), but buoy velocities were not.
 781 Hence, coincident ice velocity and 950 hPa wind speed maxima (Figure 8d-g) serve as an
 782 independent confirmation that the location of the LLJ in ERA5 is approximately correct. During
 783 the second cyclone, the cold sector LLJ core first passes over the left buoy group (Figure 8e),

Deleted: Since

Deleted: were not assimilated in ERA5

786 where drift speeds reach an average speed of 37 cm s^{-1} between 01:00 and 02:00 UTC on 1
787 February (Figure 8c) under the LLJ core of $>20 \text{ m s}^{-1}$. The DN buoys come nearly to a full stop
788 at this time before reversing direction and being accelerated by the cold sector LLJ (Figure 8c).
789 Buoys in the NW sector of the DN accelerate ahead of the cold front (Figure 8c,e, see also the
790 animations in the Supplemental Information). That is, the 2 h difference in wind and ice drift
791 direction changes and the deviations in the propagation of the ice drift reversals is most likely
792 due to internal ice stresses caused by non-local wind forcing behind the cold front. The timing
793 and direction of changes in drift direction are consistent with atmospheric stresses propagating
794 from below the cold sector LLJ as it approaches the DN. Maximum drift speeds of 42-49 cm s⁻¹
795 occur between 05:00 and 08:00 UTC on 1 February (Figure 8c) as the LLJ core passes overhead
796 (Figure 8f). There is a larger spread in velocity between the DN buoys during this time, implying
797 deformation. The DN buoys and the right group reach their maximum speeds at approximately
798 the same time (Figure 8c, f) yet due to the wind curvature within the LLJ core, the direction of
799 ice motion is different.

800 4.2 Sea ice deformation

801 Differential motion across the buoy array implies deformation. We measure this deformation by
802 monitoring the changes in polygons formed by subsets of the buoy array (Figures 9, 10) and
803 through examination of ice radar imagery (Figure 11). At moderate-to-large scales (purple,
804 yellow, and black lines and polygons in Figure 9), the largest signals in strain rates can be
805 understood as responses to the cyclone-scale wind gradients and the positions of the LLJ cores.
806 As a band of high wind speeds is advected over the ice, the ice experiences changes in vorticity,
807 divergence, and shear strain rate (Haller et al., 2014; Lindsay, 2002). For the LLJ behind the
808 storm, the vorticity pattern is first cyclonic, accompanied by gradually increasing divergence
809 (opening), then as the wind speed slows, the sense of rotation reverses, and the ice closes. This is
810 seen on 1 February both for the purple (00 to 08 UTC) and black (04-11 UTC) polygons, but at
811 slightly different times. Significant variability exists in the strain rates, particularly maximum
812 shear strain rate, likely due to the complex interaction of the geometry of ice fractures and the
813 varying wind forcing. The vorticity signal is broadly coherent (Figures 9c, 10c), with a clear
814 peak in positive vorticity at 2-3 UTC on 1 February and a trough of strongly negative vorticity
815 between 9-11 UTC on 1 February in all except the purple buoy group, which has the same

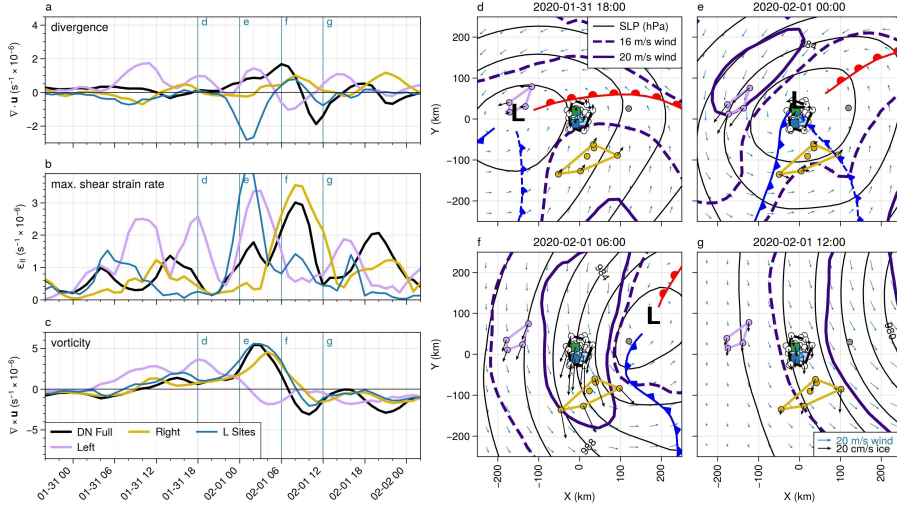
Deleted: arrival

Deleted: it appears as if

positive/negative vorticity couplet except 6–8 h earlier. The cold-sector trajectory and different timing of the position of this buoy group relative to the LLJ core seen in Figure 9d–g likely explain this time difference. This coherent positive ice-vorticity signal should be expected from the presence of the narrow axisymmetric atmospheric LLJ annulus surrounding the cyclone. The positive vorticity signal as the storm approaches is damped because the LLJs developing in the warm and cold sectors of the storm had not yet joined, and the winds ahead of the low center were weaker than the winds behind it (cf. Figure 3).

825

826



827

Figure 9. Time series of ice deformation components (a–c) and fields of 10-m winds, MSLP isobars, and 950 hPa isotachs (d–g) of the DN and Extended DN for the February 1 cyclone. Polygons used for the deformation calculations are shown in panels d–g. Polygons were selected manually. Length scales are 57 km, 40 km, and 66 km for the DN Full, Left (purple), and Right (yellow) arrays, respectively, and 18 km for the L-site array (blue).

Within the DN, the small-scale polygons generally show ice deformation consistent with the DN Full polygon, with initial positive divergence as the LLJ core approaches the polygon. The

828

829

830

831

832

833

834

835 importance of local fracture network structure in floe-floe interactions is demonstrated in the
836 broad range of divergence values, and in the outlying behavior of the L-site triangle. Considering
837 the wind field shown in Figure 9d-g and 10d-g, and the tendency of ice to move to the right of
838 the wind, we expect opening (positive divergence) while the low is centered over the DN. In
839 pack ice, individual floe motion is limited by interaction with neighboring floes, described as
840 “multifloe” (~2-10 km) and “aggregate” (10-75 km) motions in the hierarchy proposed by
841 McNutt and Overland (2003). The buoy velocity anomalies show that a region of at least 30 by
842 60 km is moving approximately coherently within the DN (Figure 10d-g). As the wind direction
843 changes, the geometry of the interlocked floes results in different regions moving as aggregates.
844 The passage of the cold sector LLJ, as indicated by the rise and fall of sea ice velocity, occurs
845 within approximately 12 hours (00-12 UTC on 1 February). Differences in the ice motion due to
846 the storm structure are visible at ~100 km (larger than “aggregate”) length scales, while
847 significant deformation is occurring at ~10 km (“multifloe”) length scales.

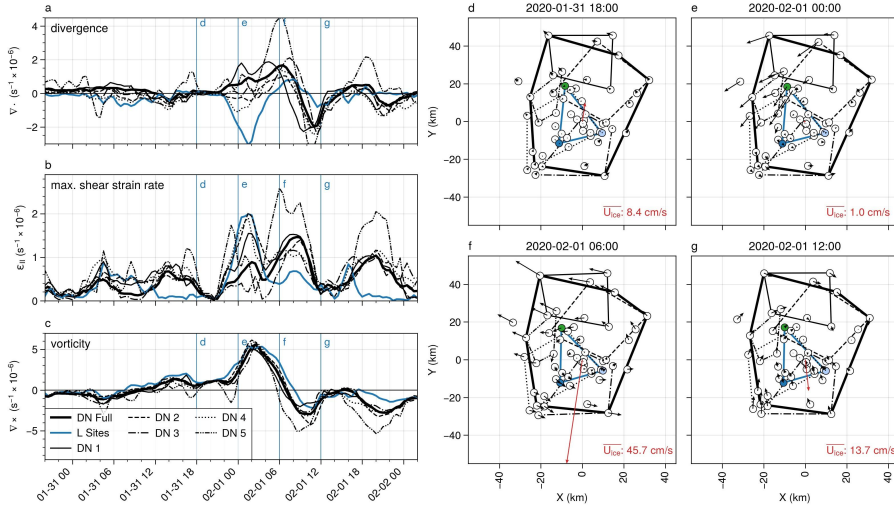
848 Remote sensing observations of ice drift are only rarely available at higher than 1 day resolution,
849 and most products have spatial resolution between 25-75 km; typically, higher spatial resolution
850 comes at a cost of smaller scenes and longer times between repeat observations (Sandven et al.,
851 2023; Wang et al., 2022). Global-scale coupled model experiments have primarily been run on
852 0.25° or coarser grids (e.g., [Long et al., 2021](#); [Selivanova et al., 2024](#); [K. E. Taylor et al., 2012](#));
853 [note that some recent regional-scale coupled models now can reach sufficiently high resolution](#)
854 [\(e.g., Huot et al., 2022\)](#). Thus, the strongest impact of the storm on the ice velocity and,
855 especially, deformation is occurring at [combined](#) time and space scales shorter and smaller than
856 [most](#) satellite ice motion observations and coupled model resolutions can resolve.

Deleted: Long et al., 2021; Taylor et al., 2012

857 Within a consolidated ice cover, there is considerable resistance to ice opening, though some
858 leads do open. As the winds recede, the newly opened leads offer little resistance to convergent
859 motion. Thus, there is considerable spread in positive divergence across the DN polygons from
860 31 January 22 UTC to approximately 9 UTC on 1 February, while convergence after that time is
861 faster and more cohesive across the set of polygons (Figure 10a). The position of shear zones can
862 lead to ambiguity in area-average strain rates, as discussed in Lindsay (2002) (see also Bouillon
863 & Rampal, 2015; Lindsay & Stern, 2003; Thorndike, 1986). The anomalous convergence shown
864 in Figure 9a and 10a for the L-site triangle is an artifact of the triangle orientation relative to a
865 shear zone that cuts through it. The shearing motion is a discontinuity in the ice velocity that

Deleted: many

leads to the triangle area to not be representative of the deformation, and compression is overestimated. The presence of this shear zone is clearly visible in the velocity anomaly map of Figure 10e. Higher confidence can be placed in the estimate of deformation from the DN Full array due to the larger number of buoys (vertices) used and larger area relative to shear zones. Over the 10-day period from 26 January 2020 to 5 February 2020, the area of the DN Full polygon changed from $3.17 \times 10^3 \text{ km}^2$ to $3.21 \times 10^3 \text{ km}^2$, a change of just over 1%. Rapid area increase (i.e., positive divergence) occurred on 1 February due to the passage of the cold sector LLJ from 00-09 UTC (Figure 10a), such that the area of the polygon increased by 3.5% in a 9-hour period, likely producing leads. Given that the surface air temperature was -10 °C or below during this period, any leads would have quickly begun freezing over. The resulting net increase of area over the 10-day period represents both thermodynamic ice growth in leads and mechanical redistribution of ice thickness in subsequent convergence.



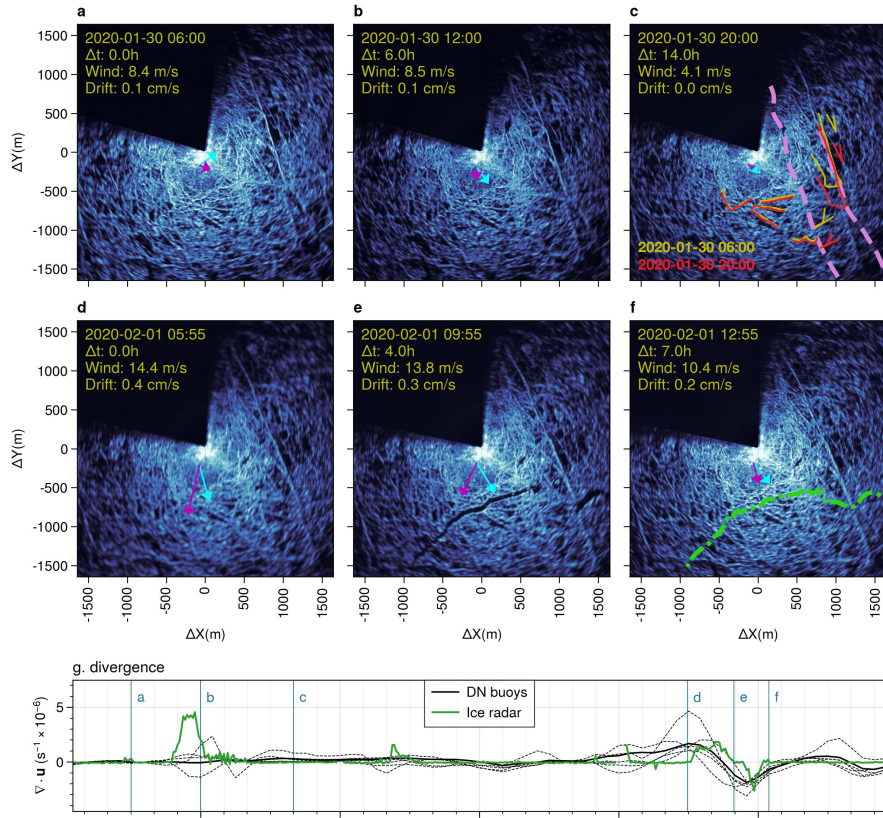
880

881 **Figure 10.** Time series of ice deformation components (a-c) and fields of buoy velocity
 882 anomalies (d-g) in the DN for the February 1 cyclone. Polygons used for the deformation
 883 calculations are shown in panels d-g; the polygons were selected manually. Note that the buoy in
 884 the upper left was not included in the DN Full array due to periods of missing data. Velocity
 885 anomalies in panels d-g were computed relative to the ensemble average velocity, which is
 886 shown as the red arrow at the center of each panel with magnitude shown in the lower right. The
 887 length scales of the polygons (square root of the average polygon area) are 28, 33, 28, 30, and 15
 888 km for DN sub-arrays 1-5 respectively, 18 km for the L-site triangle, and 57 km for the DN Full
 889 array.

890

← Formatted: Keep lines together

Deleted: ↗



893 **Figure 11.** (a-f): Backscatter from the ice radar on board the R/V Polarstern show small-scale
 894 deformation near the CO. The dark sector is blocked from the radar by the ship superstructure.
 895 Image date and time, wind speed, and drift speed are indicated in the upper left of each panel.
 896 Elapsed time (Δt) since the first image in each row is also indicated. Magenta and cyan arrows
 897 show the ice drift and wind directions at the Met City tower, respectively. Arrow length is
 898 proportional to speed; wind speed has been scaled by 2% for comparison with drift speed.
 899 Annotations in panel c show the relative movement of manually identified ice features at 30
 900 January 06 UTC (yellow) and at 20 UTC (red), revealing two prominent shear zones marked
 901 with the dashed pink lines. The green dashed line in panel f shows the location of a fracture that
 902 began opening at 1 February 07 UTC and closed by 13 UTC. (g) Sea ice divergence estimated
 903 from sea ice radar (green) and from buoys (black). Buoy deformation time series are the same as
 904 those from the DN polygons in Figure 10 and Supplemental Figure S2.

905 Ice radar images provide details of the ice deformation, ~~within ~5 km of~~ the MOSAiC CO at
 906 ~~small scales (~100 m resolution)~~. Figure 11 depicts radar backscatter intensity which is related
 907 to sea ice roughness features ~~(cropped to show details within 3 km of the CO)~~. Dark areas in
 908 radar images are interpreted as undeformed level ice or leads. High backscatter (bright areas)
 909 arises from ridges and edges of leads. Relative motion of these features or their
 910 appearance/disappearance between images indicate ice shearing, the formation of leads or ridges,
 911 or the closing of leads. Motion is readily apparent in the 15-minute resolution animations of the
 912 radar images from 25 January at 00:00 UTC and 5 February 0:00 UTC provided in the
 913 Supplement, but in some cases can be discerned in side-by-side comparisons as in Figure 11.
 914 Note that the radar is located on the roof of the bridge of the *R/V Polarstern*, located at the apex
 915 of the unsampled dark area towards the stern of the ship at the center of each image. All depicted
 916 ice motion is relative to the radar. ~~The radar images and deformation time series illustrate that~~
 917 ~~the deformation at small (< 5 km) scales is highly localized and intermittent (Weiss &~~
 918 ~~Dansereau, 2017), but also well aligned with the buoy observations (Figure 11g). The impact of~~
 919 ~~the first cyclone was manifested mainly as a six-hour long shear event with some openings.~~
 920 ~~Duration of non-negligible divergence was less than three hours.~~ The first row of images
 921 illustrates the shearing that occurred between 06:00 and 20:00 UTC on 30 January, as ~~the first~~
 922 ~~cyclone~~ passed north of the DN. During this time, the group of highlighted bright features to the
 923 right of the dashed line moved southward relative to the *R/V Polarstern* (Figure 11c). Most of the

← Formatted: Keep lines together

Deleted: 7

Deleted: around

Deleted: near

Deleted: ¶

Deleted: cyclone C₁

shear was concentrated in two regions indicated with pink dashed lines. Both shear zones had been activated at least once in the week prior. During this event, shear began at the right-most shear zone at 06:00 UTC, then along the left shear zone at 09:50 UTC. This shear zone activated again between 22:00 UTC on 31 January and 00:00 UTC as cyclone C₂ arrived, corresponding to the peak in shear near 23:00 UTC on 31 January in Figure 10b, and corresponding to the approximate time that the ice motion at the CO and L-sites reversed (Figures 6a-d).

Deleted: ing

Moved (insertion) [4]

Deleted: theon 1 February

Formatted: Subscript

The pack ice experienced opening for three hours starting at 07:00 UTC, as a fracture activates 1.5 km to the south of the R/V Polarstern (black patches in Figure 11e, green dashed line in Figure 11f, positive divergence in Figure 11g), reaching a maximum opening around 10 UTC. This time period corresponds to the latter part of the period of large atmospheric stress (Figure 5f) and the atmospheric horizontal roll vortices (Figure 4h-i). Two leads are formed with maximum width of 100-200 m, separated by a shear zone (black patches in Figure 11e). The lead closure is rapid, corresponding to a spike in convergence in the ice radar deformation time series. In contrast, divergence estimated with buoys integrates the effects of numerous fractures resulting in a relatively smooth time series that attenuates with increasing averaging scale. These local details corroborate the deformation measured with the DN buoys (Figure S2); the southward motion anomaly is coherent across a region of at least 30 by 30 km.

Moved down [5]: This time period corresponds to the period of large atmospheric stress (Figure 5f) and the atmospheric horizontal roll vortices (Figure 4h-i).

Deleted: near

Moved (insertion) [5]

Deleted: the period

Deleted: of

Deleted: ion, as carried out

Deleted: the

Deleted: ,

Deleted: results in

Deleted: ing

Moved up [4]: This shear zone activated again between 22:00 UTC on 31 January and 00:00 UTC on 1 February, corresponding to the peak in shear near 23:00 UTC on 31 January in Figure 10b, and corresponding to the approximate time that the ice motion at the CO and L-sites reversed (Figures 6a-d).

Deleted: signal

Deleted: 1

Deleted: ;

Deleted: The ice divergence maximum occurring near 06:00 UTC on 1 February in Figure 10a is also apparent in the ice radar data (Figure 11d-f). Starting at 07:00 UTC on 1 February, a fracture activates 1.5 km to the south of the R/V Polarstern (green dashed line in Figure 11f), reaching a maximum opening near 10 UTC. Two leads are formed with maximum width of 100-200 m, separated by a shear zone (black patches in Figure 11e). The leads are open only briefly, closing by 12:55 UTC. This time period corresponds to the period of large atmospheric stress (Figure 5f) and the atmospheric horizontal roll vortices (Figure 4h-i). Note that Figure 10a shows ice convergence occurring between 09:00 UTC and 13:00 UTC on 1 February, in excellent agreement with the ice radar observations. These abrupt ice motions are more easily seen in the animation of images at 15 minute resolution between 25 January at 00:00 UTC and 5 February 0:00 UTC presented in the Supplement. ¶

Deleted: together

Deleted: We therefore

Deleted: can expect that the significant transfer of momentum from the atmosphere into the sea ice results in

5 Upper ocean response to sea ice motion

Comparisons between the wind, ice and earth-reference current speeds at 8, 20 and 60 m depths (Figure 12a) summarize the transfer of momentum from the atmosphere, to the ice, and then to

1002 the ocean. This timeseries is dominated by distinct wind events on 30 and 31 January, and the
1003 strong transient event early on 1 February (Figure 12a; see also Figure 5). Each wind event
1004 accelerates the ice, which in turn accelerates the ocean layer below the ice as the turbulent ocean
1005 Ekman boundary layer forms. This can most clearly be seen in the 1 February event when wind
1006 magnitude dropped to near zero, within the annulus of the atmospheric LLJ, followed by an
1007 increase to 16 m s^{-1} in the following few hours. A local maximum ice velocity of 0.5 m s^{-1} lags
1008 the wind speed peak by 3 hours, while a 0.27 m s^{-1} current speed maximum at 8 m depth lags the
1009 ice speed maximum by ~1 hour compared to ~2 hours at 20m depth. These temporal lags are a
1010 result of the inertia of first the surface wind stress accelerating the ice, and then the depth-
1011 dependent acceleration of the upper ocean as the ice-ocean turbulent boundary layer deepens in
1012 response to changes in direction and magnitude of the ice motion.

Deleted: dropping

1013 Rapid changes in ice speed and direction during this event also force significant levels of circular
1014 inertial motion in the coupled ice-ocean system. This can be seen in the damped oscillatory
1015 current components in the north-south and east-west velocity timeseries in Figures 12c-d,
1016 starting near 1 February at 06:00 UTC and continuing for over 2 days, with the inertial ringing
1017 decaying over time. The observed ocean currents represent a superposition of inertial ringing and
1018 the evolving boundary layer currents forced by the 1 February 02:00 UTC wind event and
1019 subsequent smaller wind maxima at 12:00 UTC on 2 February and 00:00 UTC on 3 February.

1020 The inertial ringing is a resonant response to the combination of sharp transient lateral
1021 accelerations of the ice/upper ocean coupled with orthogonal Coriolis acceleration. They are
1022 widely observed in the Arctic, with higher magnitudes seen in high open water fraction
1023 conditions where ice mobility is enhanced (for example, Brenner et al., 2023). For this event, the
1024 8 m depth east-west currents track the ice motion very closely (Figure 12a) with a small phase
1025 lag and reduced current component magnitude at 20 m, while the north-south component shows
1026 an inertial response from the ice down to at least 20 m but with a larger mean boundary layer
1027 current superimposed during 1 February. As expected, there is little direct coupling of this
1028 inertial motion at depths below the seasonal (~40 m deep) mixed layer as seen in the 60 m depth
1029 time series (Figure 12a); the strong density jump at the base of the seasonal mixed layer greatly
1030 reduces mixing and hence momentum transfer to greater depths.

Deleted: the

1031 Comparison between atmospheric surface stress and 5 m ocean stress during this period (Figure
1032 12e) shows a deficit on the ocean side of the ice. There are two primary reasons for this

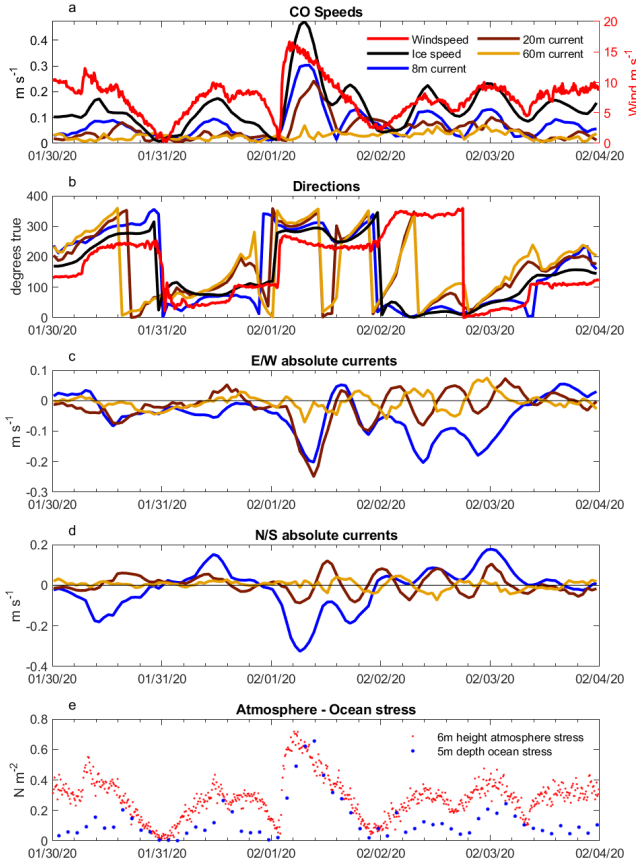
Deleted: 4

1036 difference. The first is the ability of the ice pack to remove surface-imposed momentum through
1037 a combination of internal ice stresses and ice deformation. The second is the important role of
1038 form drag from the MOSAiC ice pack. The momentum transferred by ice keels and floe edge
1039 features is not captured by the friction velocity u_0^* which arises from local upstream, small scale
1040 roughness features across the ensemble of ice floes that generates the turbulent ocean boundary
1041 layer. Lags between the peaks of atmospheric stress and ocean stress, most clearly seen in the
1042 strong 1 February event, arises from the inertial lag of the ice pack to surface wind stress (Figure
1043 12e).
1044

Deleted: and

Deleted:

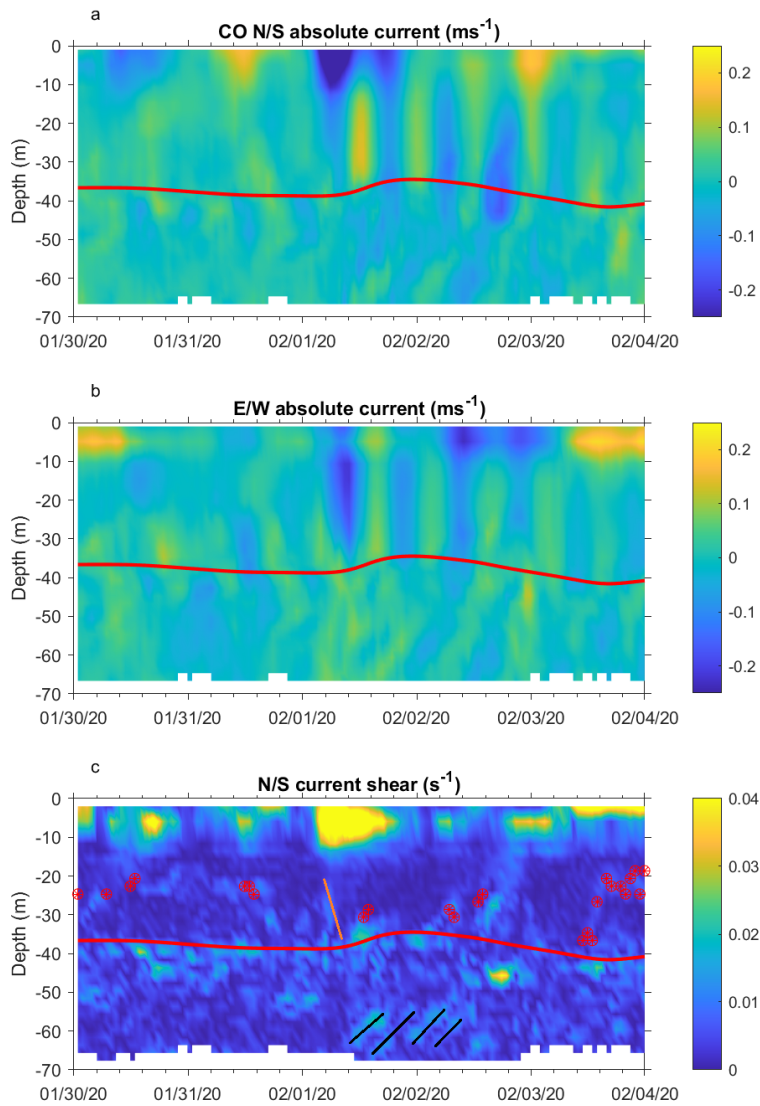
1044 The vertical structure of upper ocean currents in response to this wind event (Figure 13) illustrates the fairly complex interaction of the ice/ocean boundary layer with weakly stratified
1045 mesoscale ocean features within the seasonal mixed layer, which were seen during much of the
1046 MOSAiC transpolar drift. High temporal resolution vertical shear of the N/S current component
1047 sampled every 15 minutes by the AOFB current profiler at the CO (Figure 13c) provides some
1048 insight into the complex structure of the active mixing layer. CTD profiles were limited by wind
1049 conditions and as such are sometimes only available once per day. Ideally, CTD profiles at a
1050 comparable temporal resolution to the AOFB current profiler would show the evolution of
1051 stratification within the mixed layer, which frequently contained weak mesoscale density
1052 structures limiting the depth of mixing during wind events. However, the much higher resolution
1053 shear profile time series in Figure 13c reveal both the development of strong near-surface shear
1054 as the sub-ice Ekman layer forms, and the development of regions of higher shear within the
1055 ~40m deep seasonal mixed layer. These shear layers indicate the lower extent of the surface-
1056 forced mixing layer where even weak density gradients inhibit turbulent mixing deeper within
1057 the seasonal mixed layer. Measurements of these weak stratification layers are estimated from
1058 the depths where there is a density increase of 0.01 kg m^{-3} from surface values for each CTD
1059 profile, and are plotted as filled red circles in Figure 13c. These sparse-in-time observations
1060 coincide with the layers of increased shear measured in the current profiles. The red seasonal
1061 mixed layer depth timeseries in the Figure 13 panels represent coarse interpolated estimates of
1062 the depth of the top of the halocline.
1063



1066

067 **Figure 12.** From top to bottom: (a) Timeseries of windspeed (red), ice speed (black), 8 m (blue)
 068 20 m (brown) and 60 m (gold) depth absolute current magnitude; (b) Corresponding current and
 069 wind directions in degrees true; (c) Timeseries of 8 m (blue), 20 m (brown) and 60 m (gold)
 070 north-south current components; d) east-west current components; e) 5 m depth ocean kinematic
 071 stress from the CO site Autonomous Ocean Flux Buoy (blue dots) and atmospheric stress (red
 072 dots) for this study period.

Deleted: 5**Deleted:** green**Deleted:** orange**Deleted:** 5**Deleted:** 4



079 **Figure 13.** North-south current profile timeseries from the [CO AOFB](#) acoustic Doppler [current](#)
 1080 profiler. b) Corresponding East-West current component profiles. c) North/South current shear
 1081 profiles with a clipped color scale to emphasize shear layers within the ocean mixed layer and
 1082 upper part of the salinity-stratified pycnocline. Near surface shear reaches 0.07 s^{-1} during the 1
 1083 February wind event. [Density increases of \$0.01 \text{ kg m}^{-3}\$ above near surface values are shown as](#)
 1084 [filled red circles for each CTD profile](#). The continuous red line represents an estimate of the
 1085 depth of the top of the halocline. The sloping orange line [on 1 February](#) highlights [shear](#)
 1086 [associated with](#) rapid penetration of mixing in response to this wind event. The four black
 1087 sloping lines identify shear associated with inertial internal waves within the strongly stratified
 1088 pycnocline forced by the strong inertial motions within the ocean mixed layer.

Deleted: L1 site

Deleted: Autonomous Ocean Flux Buoy

Deleted: the

1089 The highest vertical shear levels of the north/south current component (Figure 13c) are seen in
 1090 the upper 15 m during the strong 1 February wind event. However, active [downward](#) mixing [of](#)
 1091 [momentum](#) extends [through](#) the seasonal mixed layer to the halocline, seen most clearly in the
 1092 E/W current profile (Figure 13b) and the [sloping](#) shear [layer](#) at the weak stratification interface
 1093 between 20 m depth and the halocline (marked by the orange line in Figure 13c). An example of
 1094 reduced mixing depth by a mesoscale feature, [within](#) the seasonal mixed layer is seen [with](#) the
 1095 [shoaling of the \$0.01 \text{ kg m}^{-3}\$ density jumps and shear layer](#) starting at 12:00 UTC on 2 February,
 1096 despite the continued [surface](#) [wind](#) forcing. The CO drifts over another weak stratification
 1097 feature that extends up from the pycnocline [starting at 14:00 UTC on 3 February](#). The interplay
 1098 between surface mixing and these frequent mesoscale features with a wide range of density
 1099 gradient strengths observed during the MOSAiC drift complicates a 1D view of wind-forced
 1100 turbulent momentum transfer into the ocean. Analysis of these mesoscale features is beyond the
 1101 scope of the present paper, and [is being](#) explored in [other analyses](#).

Deleted: down

Deleted: elimination of

Deleted: at the base of the

Deleted: 1

Formatted: Superscript

Deleted: strong

Deleted: as winds reduce to 3 m s^{-1} at 00:00 UTC on 2 February...

Deleted: will

Deleted: subsequent publications

Deleted: shown as

Deleted: These i

1102 Strong inertial-period motions in the ocean mixed layer are capable of generating internal
 1103 inertial-period waves within the pycnocline after the mixing layer inertial currents contact the
 1104 strongly salinity-stratified pycnocline. In the current component profiles (Figures 13a and 13b)
 1105 this can be seen as slanted bands of enhanced current shear with inertial periods starting around
 1106 45 m depth after the 1 February wind event. These regions of enhanced shear are also
 1107 [emphasized by the black slanting lines](#) in Figure 13c. [Inertial](#) [internal](#) waves are an important
 1108 source of shear that can induce mixing in the otherwise very quiescent and non-diffusive Arctic
 1109 pycnocline. [The damped resonant inertial motions in the ice and ocean mixing layer transport](#)

124 and dissipate wind-forced momentum after the strong transient event on 1 February. The
125 momentum is gradually transferred over several days into the halocline as inertial motions that in
126 turn form these inertial internal waves that propagate into the ocean interior (for example, see
127 [Guthrie & Morison, 2021](#))

1128

1129 **6 Discussion and conclusions**

1130 We presented a detailed description of an observed, strong, mid-winter, central Arctic cyclone
1131 which passed over the MOSAiC observatory from 31 January to 1 February 2020, closely
1132 following the passage of a weaker cyclone. This cyclone included the development and passage
1133 of a strong quasi-axisymmetric low-level jet (LLJ) in the lower atmosphere, produced
1134 widespread sea ice deformation, and propagated momentum flux into the upper ocean. The
1135 comprehensive suite of MOSAiC instruments together provides unique observations of the
1136 coupled air-ice-ocean system during an evolving cyclone with unprecedented detail and spatial
1137 resolution.

1138 The sea ice response to the cyclone occurs across scales. At the scale of the cyclone, local sea ice
1139 trajectories are a function of position relative to the storm track. The strongest impacts of the
1140 cyclone are associated with mesoscale features. The developing atmospheric LLJ, which
1141 eventually appears as an annulus of ~140 km radius around the low-pressure center, is the key
1142 atmospheric feature of this cyclone impacting the momentum transfer to the sea ice. A smaller jet
1143 core within this LLJ is identified in the cold sector of the ERA5 reanalyses between 00 and 12
1144 UTC on 1 February, and is linked to observed faster ice motion as well as shearing and
1145 divergence of the sea ice. The stage of storm development and the spatial structure of the LLJ
1146 strongly impacted the timing and location of sea ice deformation. The elevated surface wind
1147 speeds ahead of the cyclone produced an increase in drift speed and resulted in ice shear. The
1148 developed LLJ behind the cold front produced strong deformation in the ice, with divergence
1149 ahead of the jet core and convergence behind. This produced opening and closing of leads,
1150 respectively. The sudden change in wind and ice-drift direction and the rapid increase in sea ice
1151 velocity with the arrival of the cold-sector LLJ and its core produced a jump in the air-ice and
1152 ice-ocean stresses. The local destabilization of the lower atmosphere behind the cold front
1153 contributed to the former, while the latter initiated an inertial oscillation in the sea ice and upper

Deleted: produced air-ice-ocean changes, including leading to ...

Deleted: ing

Deleted: ing

Moved (insertion) [7]

Deleted: L

Deleted: distance to the

Deleted: and the side of the track

Moved up [7]: Local sea ice trajectories are a function of distance to the storm track and the side of the track.

1163 ocean. The observations also showed that the change in ice-drift direction occurred locally in the
1164 DN about 2 h prior to the change in wind direction with the cold front, suggesting that wind
1165 forcing of the ice behind the cold front propagated ahead of the front through the internal ice
1166 stress. Hence, wind forcing of ice acceleration may not always occur locally.

1167 The initiation of the inertial oscillation in the ocean extended the impacts of the storm beyond the
1168 time taken for the atmospheric depression to fully cross the observatory. A second increase in sea
1169 ice strain rates 12 hours after the arrival of the LLJ occurred due to the differing timescales
1170 between the atmosphere and the coupled ice-ocean boundary layer during the inertial oscillation
1171 and the gradual change in the wind direction. The ice and near-surface ocean returned to
1172 following the wind after approximately 24 hours, while at depth, the effects of the inertial
1173 oscillation were visible for at least 3 days. [Thus, even in the Central Arctic ice pack during](#)
1174 [winter, ice-ocean momentum transport in response to the mesoscale features of an atmospheric](#)
1175 [cyclone can significantly impact mixing in the upper ocean.](#)

1176 Because of the apparent importance of the LLJ and the LLJ core for air-ice interactions, it must
1177 be noted that there is some uncertainty in its spatial and temporal structure. Since it was only
1178 directly observed by the 1 February 06:00 UTC sounding, and temporally and spatially spread by
1179 the ERA5 data assimilation, there could have been other LLJ cores or this core could have been
1180 present before 1 February 00:00 UTC. However, no atmospheric or ice observations suggest this
1181 to be the case. Furthermore, the structure and strength of the LLJ in the warm sector is also not
1182 well observed, as the 31 January 18:00 UTC sounding only captures the inner edge of the LLJ
1183 annulus at a time when the axisymmetric characteristic has not yet developed (Figure 3a). Hence,
1184 to describe the LLJ structure we use ERA5 to fill time and space between observations. [Though](#)
1185 [some recent Arctic cyclone structure studies have mentioned the presence of strong low-level](#)
1186 [winds in the warm sector \(e.g., Vessey et al., 2022\), LLJs have not been a part of the classical](#)
1187 [conceptual models of Arctic cyclones \(e.g., Aizawa & Tanaka, 2016\), likely due to the lack of](#)
1188 [observations or reanalyses capable of resolving such mesoscale features. Furthermore, to our](#)
1189 [knowledge, no studies, other than Persson et al. \(2023\), have previously mentioned the possible](#)
1190 [key role of wrap-around or dual LLJs for impacting sea ice deformation.](#)

1191 The breadth of observation types available through the MOSAiC observatory provides
1192 opportunity for numerical model evaluation and development, enabling examination of multi-

Deleted:

Deleted: Finally,

Deleted: these studies relying on

Deleted: with a resolution incapable

Deleted: -

Deleted: . More recent Arctic cyclone structure studies using ERA5 (e.g., Vessey et al., 2022), have mentioned the presence of strong low-level winds in the warm sector, however. More details of the LLJ structure for this storm and other MOSAiC cyclones may be available from the surface-based remote sensors at MOSAiC, such as wind lidars and wind profilers with temporal resolution much finer than 6 h, and may be topics of future studies.

1206 scale, strongly coupled processes. While numerous case studies of cyclones exist, most focus on
1207 the summer and the marginal ice zone. Few observations are available for the central Arctic in
1208 full pack ice during mid-winter. We have identified key processes for the transfer of energy from
1209 atmosphere to sea ice to the upper ocean. A companion study will examine the representation of
1210 these processes in modern coupled air-ice-ocean numerical weather forecast models. [Other future](#)
1211 [studies will examine the generality of the results of this paper through studies of other MOSAiC](#)
1212 [cyclones. Such studies could also reveal whether there is a role in cyclone interactions where one](#)
1213 [cyclone can precondition the ice for enhanced air-ice-ocean interactions during subsequent](#)
1214 [cyclones.](#)

Deleted: , such as the cyclone encountered two days prior to the 1 February cyclone

Deleted: sequential training of cyclones preconditions the

Deleted: for

1215 Acknowledgments

1216 DW, OP, AS, and JKH were funded by the US Department of Energy (DoE), under grant ←
1217 DE-SC0021342. The participation of TS was funded through the National Science Foundation
1218 (NSF) OPP1723400. [JH's contribution was funded by the European Union's Horizon 2020](#)
1219 [research and innovation program under grant agreement No. 101003826 via the project CRiceS](#)
220 [\(Climate Relevant interactions and feedbacks: the key role of sea ice and Snow in the polar and](#)
221 [global climate system.\)](#) Atmospheric measurements and data processing were supported by NSF
1222 grant OPP1724551 and the DoE Atmospheric Radiation Measurement Program. The deployment
1223 of GPS ice drifters and coordination within the MOSAiC DN was funded by NSF 1722729. OP
1224 also received support from the Office of Naval Research grant ONR 1564162 during the
1225 preparation of this manuscript. [The Ice-Tethered Profiler data were collected and made available](#)
226 [by the Ice-Tethered Profiler Program \(Krishfield et al., 2008; J. Toole et al., 2011\) based at the](#)
227 [Woods Hole Oceanographic Institution \(<https://www2.whoi.edu/site/itp/>\)](#)

Formatted: Indent: First line: 0.5"

1228 We acknowledge the group effort required for the success of the MOSAiC expedition (Nixdorf et
1229 al., 2021). We additionally thank the MOSAiC distributed network team for additional GPS ice
1230 drift data and coordination of the L-sites and buoy deployments; the MOSAiC atmosphere team
1231 for supporting data collection during the MOSAiC field campaign, running instruments in the
1232 CO and maintaining the ASFS at L-sites; and the MOSAiC sea ice and snow team on MOSAiC
1233 Leg 2, in particular Polona Itkin, for supporting the ice radar data collection. [In addition, we](#)
1234 [thank Matias Uusinoka for his provision of the ice radar-derived deformation time series.](#) The
1235 authors do not perceive any conflicts of interest.

1240

1241 **Open Research**

1242 Atmospheric and ice drift data used in this paper are archived at the Arctic Data Center (Sea ice
1243 buoys: Bliss et al., 2022; atmospheric data: Cox et al., (2023a-d) and in the Alfred Wegner
1244 Institute PANGAEA archive (Maturilli et al., 2022). Atmospheric Ka-band radar is archived at
1245 the Department of Energy Atmospheric Radiation Measurement User Facility (Bharadwaj et al.,
1246 2019; Hardin et al., 2019). Ice radar data is archived in the Alfred Wegner Institute PANGAEA
1247 archive (Krumpen et al., 2021a). Data from the Autonomous Ocean Flux Buoy is archived at the
1248 Arctic Data Center (Stanton & Shaw, 2023). Code supporting the data analysis and visualization
1249 is archived at Zenodo (<https://doi.org/10.5281/zenodo.10698905>).

1250

1251 **References**

- 1252 [Aizawa, T., & Tanaka, H. L. \(2016\). Axisymmetric structure of the long lasting summer Arctic cyclones. *Polar*](#)
1253 [Science, 10\(3\), 192–198. https://doi.org/10.1016/j.polar.2016.02.002](#)
- 1254 [Andreas, E. L., Horst, T. W., Grachev, A. a., Persson, P. O. G., Fairall, C. W., Guest, P. S., & Jordan, R. E. \(2010\).](#)
1255 [Parametrizing turbulent exchange over summer sea ice and the marginal ice zone. *Quarterly Journal of the*](#)
1256 [Royal Meteorological Society, 136\(March\), 927–943. https://doi.org/10.1002/qj.618](#)
- 1257 [Andreas, E. L., Persson, P. O. G., Grachev, A. a., Jordan, R. E., Horst, T. W., Guest, P. S., & Fairall, C. W. \(2010\).](#)
1258 [Parameterizing Turbulent Exchange over Sea Ice in Winter. *Journal of Hydrometeorology, 11\(1\), 87–104.*](#)
1259 [https://doi.org/10.1175/2009JHM1102.1](#)
- 1260 [Aue, L., Vihma, T., Uotila, P., & Rinke, A. \(2022\). New Insights Into Cyclone Impacts on Sea Ice in the Atlantic](#)
1261 [Sector of the Arctic Ocean in Winter. *Geophysical Research Letters, 49\(22\).*](#)
1262 [https://doi.org/10.1029/2022GL100051](#)
- 1263 [Bharadwaj, N., Hardin, J., Isom, B., Johnson, K., Lindenmaier, I., Matthews, A., Nelson, D., Feng, Y.-C., Deng, M.,](#)
1264 [Rocque, M., Castro, V., & Giangrande, T. \(2019\). *Ka-Band Scanning ARM Cloud Radar \(KASACRCFR\).*](#)
1265 [2020-01-29 to 2020-02-04, ARM Mobile Facility \(MOS\) MOSAIC \(Drifting Obs—Study of Arctic Climate\);](#)
1266 [AMF2 \(M1\) \[dataset\]. Atmospheric Radiation Measurement \(ARM\) user facility.](#)
1267 [http://dx.doi.org/10.5439/1615726](#)

- 268 Bliss, A. C., Hutchings, J. K., Anderson, P., Anhaus, P., Belter, H. J., Berge, J., Bessonov, V., Cheng, B., Cole, S.,
269 Costa, D., Cottier, F., Cox, C. J., de la Torre, R., Divine, D., Emzivat, G., Fang, Y. C., Fons, S., Gallagher,
270 M., Geoffrey, M., ... Zuo, G. (2022). *Sea ice drift tracks from the Distributed Network of autonomous*
271 *buoys deployed during the Multidisciplinary drifting Observatory for the Study of Arctic Climate*
272 (*MOSAiC*) *expedition 2019–2021* [dataset]. Arctic Data Center. doi:10.18739/A2KP7TS83
- 273 Bliss, A. C., Hutchings, J. K., & Watkins, D. M. (2023). Sea ice drift tracks from autonomous buoys in the MOSAiC
274 *Distributed Network*. *Scientific Data*, 10(403), 1–10. <https://doi.org/10.1038/s41597-023-02311-y>
- 275 Bouillon, S., & Rampal, P. (2015). On producing sea ice deformation data sets from SAR-derived sea ice motion.
276 *The Cryosphere*, 9(2), 663–673. <https://doi.org/10.5194/tc-9-663-2015>
- 277 Brenner, S., Thomson, J., Rainville, L., Crews, L., & Lee, C. M. (2023). Wind-Driven Motions of the Ocean Surface
278 Mixed Layer in the Western Arctic. *Journal of Physical Oceanography*, 53(7), 1787–1804.
279 <https://doi.org/10.1175/JPO-D-22-0112.1>
- 280 Brümmer, B. (2003). A Fram Strait cyclone: Properties and impact on ice drift as measured by aircraft and buoys.
281 *Journal of Geophysical Research*, 108(D7), 4217. <https://doi.org/10.1029/2002JD002638>
- 282 Brümmer, B., & Hoeber, H. (1999). A mesoscale cyclone over the Fram Strait and its effects on sea ice. *Journal of*
283 *Geophysical Research: Atmospheres*, 104(D16), 19085–19098. <https://doi.org/10.1029/1999JD900259>
- 284 Brümmer, B., Schröder, D., Müller, G., Spreen, G., Jahnke-Bornemann, A., & Launiainen, J. (2008). Impact of a
285 Fram Strait cyclone on ice edge, drift, divergence, and concentration: Possibilities and limits of an
286 observational analysis. *Journal of Geophysical Research: Oceans*, 113(12), 1–15.
287 <https://doi.org/10.1029/2007JC004149>
- 288 Carlson, T. N. (1980). Airflow through midlatitude cyclones and the comma cloud pattern. *Monthly Weather*
289 *Review*, 108, 1498–1509. [https://doi.org/10.1175/1520-0493\(1980\)108<1498:ATMCAT>2.0.CO;2](https://doi.org/10.1175/1520-0493(1980)108<1498:ATMCAT>2.0.CO;2)
- 290 Clancy, R., Bitz, C. M., Blanchard-Wrigglesworth, E., McGraw, M. C., & Cavallo, S. M. (2022). A cyclone-
291 centered perspective on the drivers of asymmetric patterns in the atmosphere and sea ice during Arctic
292 cyclones. *Journal of Climate*, 1–47. <https://doi.org/10.1175/JCLI-D-21-0093.1>
- 293 Cox, C., Gallagher, M., Shupe, M., Blomquist, B., Persson, O., Grachev, A., Riihimaki, L. D., Kuchenreiter, M.,
294 Morris, V., Solomon, A., Brooks, I., Costa, D., Gottas, D., Hutchings, J. K., Osborn, J., Morris, S. M.,
295 Preusser, A., & Uttal, T. (2023). *Met City meteorological and surface flux measurements (Level 3 Final)*.

- 296 [Multidisciplinary Drifting Observatory for the Study of Arctic Climate \(MOSAiC\), central Arctic, October](#)
297 [2019–September 2020 \[dataset\]. Arctic Data Center. https://doi.org/10.18739/A2PV6B83F](#)
- 298 [Cox, C., Gallagher, M., Shupe, M., Persson, O., Grachev, A., Solomon, A., Ayers, T., Costa, D., Hutchings, J. K.,](#)
299 [Leach, J., Morris, S. M., Osborn, J., Pezoa, S., & Uttal, T. \(2023a\). Atmospheric Surface Flux Station #30](#)
300 [measurements \(Level 3 Final\), Multidisciplinary Drifting Observatory for the Study of Arctic Climate](#)
301 [\(MOSAiC\), central Arctic, October 2019–September 2020 \[dataset\]. Arctic Data Center.](#)
302 [https://doi.org/10.18739/A2FF3M18K](#)
- 303 [Cox, C., Gallagher, M., Shupe, M., Persson, O., Grachev, A., Solomon, A., Ayers, T., Costa, D., Hutchings, J. K.,](#)
304 [Leach, J., Morris, S. M., Osborn, J., Pezoa, S., & Uttal, T. \(2023b\). Atmospheric Surface Flux Station #40](#)
305 [measurements \(Level 3 Final\), Multidisciplinary Drifting Observatory for the Study of Arctic Climate](#)
306 [\(MOSAiC\), central Arctic, October 2019–September 2020 \[dataset\]. Arctic Data Center.](#)
307 [https://doi.org/10.18739/A2FF3M18K](#)
- 308 [Cox, C., Gallagher, M., Shupe, M., Persson, O., Grachev, A., Solomon, A., Ayers, T., Costa, D., Hutchings, J. K.,](#)
309 [Leach, J., Morris, S. M., Osborn, J., Pezoa, S., & Uttal, T. \(2023c\). Atmospheric Surface Flux Station #50](#)
310 [measurements \(Level 3 Final\), Multidisciplinary Drifting Observatory for the Study of Arctic Climate](#)
311 [\(MOSAiC\), central Arctic, October 2019–September 2020 \[dataset\]. Arctic Data Center.](#)
312 [https://doi.org/10.18739/A2XD0R00S](#)
- 313 [Cox, C. J., Gallagher, M. R., Shupe, M. D., Persson, P. O. G., Solomon, A., Fairall, C. W., Ayers, T., Blomquist, B.,](#)
314 [Brooks, I. M., Costa, D., Grachev, A., Gottas, D., Hutchings, J. K., Kutchener, M., Leach, J., Morris, S.](#)
315 [M., Morris, V., Osborn, J., Pezoa, S., ... Uttal, T. \(2023\). Continuous observations of the surface energy](#)
316 [budget and meteorology over the Arctic sea ice during MOSAiC. Scientific Data, 10\(1\), 519.](#)
317 [https://doi.org/10.1038/s41597-023-02415-5](#)
- 318 [Deser, C., Tomas, R. A., & Sun, L. \(2015\). The role of ocean-atmosphere coupling in the zonal-mean atmospheric](#)
319 [response to Arctic sea ice loss. Journal of Climate, 28\(6\), 2168–2186. https://doi.org/10.1175/JCLI-D-14-](#)
320 [00325.1](#)
- 321 [Etling, D., & Brown, R. A. \(1993\). Roll vortices in the planetary boundary layer: A review. Boundary-Layer](#)
322 [Meteorology, 65\(3\), 215–248. https://doi.org/10.1007/BF00705527](#)

- 323 [Fearon, M. G., Doyle, J. D., Ryglicki, D. R., Finocchio, P. M., & Sprenger, M. \(2021\). The Role of Cyclones in](#)
324 [Moisture Transport into the Arctic. *Geophysical Research Letters*, 48\(4\), e2020GL090353.](#)
325 <https://doi.org/10.1029/2020GL090353>
- 326 [Fer, I., Baumann, T. M., Koenig, Z., Muilwijk, M., & Tippenhauer, S. \(2022\). Upper-Ocean Turbulence Structure](#)
327 [and Ocean-Ice Drag Coefficient Estimates Using an Ascending Microstructure Profiler During the](#)
328 [MOSAiC Drift. *Journal of Geophysical Research: Oceans*, 127\(9\). https://doi.org/10.1029/2022JC018751](#)
- 329 [Gallaher, S. G., Stanton, T. P., Shaw, W. J., Cole, S. T., Toole, J. M., Wilkinson, J. P., Maksym, T., & Hwang, B.](#)
330 [\(2016\). Evolution of a Canada Basin ice-ocean boundary layer and mixed layer across a developing](#)
331 [thermodynamically forced marginal ice zone. *Journal of Geophysical Research: Oceans*, 121\(8\), 6223–](#)
332 [6250. https://doi.org/10.1002/2016JC011778](https://doi.org/10.1002/2016JC011778)
- 333 [Gimbert, F., Marsan, D., Weiss, J., Jourdain, N. C., & Barnier, B. \(2012\). Sea ice inertial oscillations in the Arctic](#)
334 [Basin. *The Cryosphere*, 6\(5\), 1187–1201. https://doi.org/10.5194/tc-6-1187-2012](#)
- 335 [Grachev, A. A., Andreas, E. L., Fairall, C. W., Guest, P. S., & Persson, P. O. G. \(2007\). SHEBA flux-profile](#)
336 [relationships in the stable atmospheric boundary layer. *Boundary-Layer Meteorology*, 124\(3\), 315–333.](#)
337 <https://doi.org/10.1007/s10546-007-9177-6>
- 338 [Graham, R. M., Cohen, L., Ritzhaupt, N., Segger, B., Graversen, R. G., Rinke, A., Walden, V. P., Granskog, M. A.,](#)
339 [& Hudson, S. R. \(2019\). Evaluation of six atmospheric reanalyses over Arctic sea ice from winter to early](#)
340 [summer. *Journal of Climate*, 32\(14\), 4121–4143. https://doi.org/10.1175/JCLI-D-18-0643.1](#)
- 341 [Graham, R. M., Hudson, S. R., & Maturilli, M. \(2019\). Improved performance of ERA5 in Arctic gateway relative](#)
342 [to four global atmospheric reanalyses. *Geophysical Research Letters*, 46\(11\), 6138–6147.](#)
343 <https://doi.org/10.1029/2019GL082781>
- 344 [Guthrie, J. D., & Morison, J. H. \(2021\). Not Just Sea Ice: Other Factors Important to Near-inertial Wave Generation](#)
345 [in the Arctic Ocean. *Geophysical Research Letters*, 48\(3\), e2020GL090508.](#)
346 <https://doi.org/10.1029/2020GL090508>
- 347 [Haapala, J., Lönnroth, N., & Stössel, A. \(2005\). A numerical study of open water formation in sea ice. *Journal of*](#)
- 348 [*Geophysical Research*, 110\(C9\), C09011. https://doi.org/10.1029/2003JC002200](#)

- 349 [Haller, M., Brümmer, B., & Müller, G. \(2014\). Atmosphere–ice forcing in the transpolar drift stream: Results from](#)
350 [the DAMOCLES ice-buoy campaigns 2007–2009. *The Cryosphere*, 8\(1\), 275–288.](#)
351 <https://doi.org/10.5194/tc-8-275-2014>
- 352 [Hardin, J., Hunzinger, A., Schuman, E., Matthews, A., Bharadwaj, N., Varble, A., Johnson, K., Giangrande, S.,](#)
353 [Feng, Y.-C., & Lindenmaier, I. \(2019\). *Ka ARM Zenith Radar \(KAZRCFRGEQC\). 2020-01-29 to 2020-02-*](#)
354 [05. ARM Mobile Facility \(MOS\) MOSAIC \(Drifting Obs—Study of Arctic Climate\); AMF2 \(M1\).](#)
355 [Atmospheric Radiation Measurement \(ARM\) user facility. https://doi.org/10.5439/1615726](#)
- 356 [Hersbach, H., Bell, B., Berrisford, P., Biavati, G., Horányi, A., Muñoz Sabater, J., Nicolas, J., Radu, C., Rozum, I.,](#)
357 [Schepers, D., Simmons, A., Soci, C., Dee, D., & Thépaut, J. \(2023a\). *ERA5 hourly data on pressure levels*](#)
358 [from 1940 to present. \[dataset\]. Copernicus Climate Change Service \(C3S\) Climate Data Store \(CDS\).](#)
359 <https://doi.org/10.24381/cds.bd0915c6>
- 360 [Hersbach, H., Bell, B., Berrisford, P., Biavati, G., Horányi, A., Muñoz Sabater, J., Nicolas, J., Radu, C., Rozum, I.,](#)
361 [Schepers, D., Simmons, A., Soci, C., Dee, D., & Thépaut, J. \(2023b\). *ERA5 hourly data on single levels*](#)
362 [from 1940 to present. \[dataset\]. Copernicus Climate Change Service \(C3S\) Climate Data Store \(CDS\).](#)
363 <https://doi.org/10.24381/cds.adbb2d47>
- 364 [Hersbach, H., Bell, B., Berrisford, P., Hirahara, S., Horányi, A., Nicolas, J., Peubey, C., Radu, R., Bonavita, M.,](#)
365 [Dee, D., Dragani, R., Flemming, J., Forbes, R., Geer, A., Hogan, R. J., Janisková, H. M., Keeley, S.,](#)
366 [Laloyaux, P., Cristina, P. L., & Thépaut, J. \(2020\). The ERA5 global reanalysis. *Quarterly Journal of the*](#)
367 [Royal Meteorological Society, June, 1999–2049. https://doi.org/10.1002/qj.3803](#)
- 368 [Hessner, El Naggar, Von Appen, & Strass. \(2019\). On the Reliability of Surface Current Measurements by X-band](#)
369 [Marine Radar. *Remote Sensing*, 11\(9\), 1030. https://doi.org/10.3390/rs11091030](#)
- 370 [Hibler, W. D. \(1979\). A Dynamic Thermodynamic Sea Ice Model. *Journal of Physical Oceanography*, 9\(4\), 815–](#)
371 [846. https://doi.org/10.1175/1520-0485\(1979\)009<0815:ADTSIM>2.0.CO;2](https://doi.org/10.1175/1520-0485(1979)009<0815:ADTSIM>2.0.CO;2)
- 372 [Hunke, E. C., Lipscomb, W. H., Turner, A. K., Jeffery, N., & Elliott, S. \(2015\). *CICE : the Los Alamos Sea Ice*](#)
373 [Model Documentation and Software User's Manual \[Computer software\].](#)
- 374 [Hunkins, K. \(1967\). Inertial oscillations of Fletcher's Ice Island \(T-3\). *Journal of Geophysical Research*, 72\(4\),](#)
375 [1165–1174. https://doi.org/10.1029/JZ072i004p01165](https://doi.org/10.1029/JZ072i004p01165)

- 376 [Huot, P.-V., Kittel, C., Fichefet, T., Jourdain, N. C., & Fettweis, X. \(2022\). Effects of ocean mesoscale eddies on](#)
377 [atmosphere–sea ice–ocean interactions off Adélie Land, East Antarctica. *Climate Dynamics*, 59\(1–2\), 41–](#)
378 [60. <https://doi.org/10.1007/s00382-021-06115-x>](#)
- 379 [Hutchings, J. K., Heil, P., Steer, A., & Hibler, W. D. \(2012\). Subsynoptic scale spatial variability of sea ice](#)
380 [deformation in the western Weddell Sea during early summer. *Journal of Geophysical Research*, 117\(C1\),](#)
381 [C01002. <https://doi.org/10.1029/2011JC006961>](#)
- 382 [Hutchings, J. K., Roberts, A., Geiger, C. A., & Richter-Menge, J. \(2011\). Spatial and temporal characterization of](#)
383 [sea-ice deformation. *Annals of Glaciology*, 52\(57 PART 2\), 360–368.](#)
384 [https://doi.org/10.3189/172756411795931769](#)
- 385 [Hutchings, J. K., Roberts, A., Geiger, C. A., & Richter-Menge, J. \(2018\). Corrigendum: Spatial and temporal](#)
386 [characterisation of sea-ice deformation. *Journal of Glaciology*, 64\(244\), 343–346.](#)
387 [https://doi.org/10.1017/jog.2018.11](#)
- 388 [Itkin, P., Spreen, G., Cheng, B., Doble, M., Girard-Ardhuin, F., Haapala, J., Hughes, N., Kaleschke, L., Nicolaus,](#)
389 [M., & Wilkinson, J. \(2017\). Thin ice and storms: Sea ice deformation from buoy arrays deployed during N-](#)
390 [ICE2015. *Journal of Geophysical Research: Oceans*, 122\(6\), 4661–4674.](#)
391 [https://doi.org/10.1002/2016JC012403](#)
- 392 [Jozef, G. C., Cassano, J. J., Dahlke, S., Dice, M., Cox, C. J., & De Boer, G. \(2023\). Thermodynamic and kinematic](#)
393 [drivers of atmospheric boundary layer stability in the central Arctic during the Multidisciplinary drifting](#)
394 [Observatory for the Study of Arctic Climate \(MOSAiC\). *Atmospheric Chemistry and Physics*, 23\(20\),](#)
395 [13087–13106. <https://doi.org/10.5194/acp-23-13087-2023>](#)
- 396 [Kaimal, J. C., & Finnigan, J. J. \(1994\). *Atmospheric boundary layer flows: Their structure and measurement*.](#)
397 [Oxford University Press. <https://doi.org/10.1093/oso/9780195062397.001.0001>](#)
- 398 [Kriegsmann, A., & Brümmer, B. \(2014\). Cyclone impact on sea ice in the central Arctic Ocean: A statistical study.](#)
399 [The *Cryosphere*, 8\(1\), 303–317. <https://doi.org/10.5194/tc-8-303-2014>](#)
- 400 [Krishfield, R., Toole, J., Proshutinsky, A., & Timmermans, M.-L. \(2008\). Automated Ice-Tethered Profilers for](#)
401 [Seawater Observations under Pack Ice in All Seasons. *Journal of Atmospheric and Oceanic Technology*,](#)
402 [25\(11\), 2091–2105. <https://doi.org/10.1175/2008JTECHO587.1>](#)

- 403 [Krumpen, T., Birrien, F., Kauker, F., Rackow, T., von Albedyll, L., Angelopoulos, M., Belter, H. J., Bessonov, V.,](#)
404 [Damm, E., Dethloff, K., Haapala, J., Haas, C., Hendricks, S., Hoelemann, J., Hopmann, M., Kaleschke,](#)
405 [L., Karcher, M., Kolabutin, N., Lenz, J., ... Watkins, D. M. \(2020\). The MOSAiC ice floe: Sediment-laden](#)
406 [survivor from the Siberian shelf. *The Cryosphere*, 14, 2173–2187. <https://doi.org/10.5194/tc-2020-64>](#)
- 407 [Krumpen, T., Haapala, J., Krocker, R., & Bartsch, A. \(2021\). *Ice radar raw data \(sigma S6 ice radar\) of RV*](#)
408 [POLARSTERN during cruise PS122/I. PANGAEA / Alfred Wegener Institute, Helmholtz Centre for Polar](#)
409 [and Marine Research, Bremerhaven. <https://doi.org/10.1594/PANGAEA.929434>](#)
- 410 [Krumpen, T., von Albedyll, L., Goessling, H. F., Hendricks, S., Juhls, B., Spreen, G., Willmes, S., Belter, H. J.,](#)
411 [Dethloff, K., Haas, C., Kaleschke, L., Katlein, C., Tian-Kunze, X., Ricker, R., Rostosky, P., Rückert, J.,](#)
412 [Singha, S., & Sokolova, J. \(2021\). MOSAiC drift expedition from October 2019 to July 2020: Sea ice](#)
413 [conditions from space and comparison with previous years. *The Cryosphere*, 15\(8\), 3897–3920.](#)
414 <https://doi.org/10.5194/tc-15-3897-2021>
- 415 [Kwok, R., Spreen, G., & Pang, S. \(2013\). Arctic sea ice circulation and drift speed: Decadal trends and ocean](#)
416 [currents. *Journal of Geophysical Research: Oceans*, 118\(5\), 2408–2425. <https://doi.org/10.1002/jgrc.20191>](#)
- 417 [Lei, R., Gui, D., Heil, P., Hutchings, J. K., & Ding, M. \(2020\). Comparisons of sea ice motion and deformation, and](#)
418 [their responses to ice conditions and cyclonic activity in the western Arctic Ocean between two summers.](#)
419 [Cold Regions Science and Technology, 170\(November 2018\), 102925.](#)
420 <https://doi.org/10.1016/j.coldregions.2019.102925>
- 421 [LeMone, M. A. \(1973\). The Structure and Dynamics of Horizontal Roll Vortices in the Planetary Boundary Layer.](#)
422 [Journal of the Atmospheric Sciences, 30, 1077–1091. \[https://doi.org/10.1175/1520-0469\\(1973\\)030<1077:TSADOH>2.0.CO;2\]\(https://doi.org/10.1175/1520-0469\(1973\)030<1077:TSADOH>2.0.CO;2\)](#)
- 423 [Leppäranta, M. \(2011\). *The Drift of Sea Ice* \(2nd ed.\). Springer-Verlag Berlin Heidelberg.](#)
424 <https://doi.org/10.1007/978-3-642-04683-4>
- 425 [Lindsay, R. W. \(2002\). Ice deformation near SHEBA. *Journal of Geophysical Research*, 107\(C10\), 8042.](#)
426 <https://doi.org/10.1029/2000JC000445>
- 427 [Lindsay, R. W., & Stern, H. L. \(2003\). The RADARSAT Geophysical Processor System: Quality of sea ice](#)
428 [trajectory and deformation estimates. *Journal of Atmospheric and Oceanic Technology*, 20\(9\), 1333–1347.](#)
429 [https://doi.org/10.1175/1520-0426\(2003\)020<1333:TRGAPSQ>2.0.CO;2](https://doi.org/10.1175/1520-0426(2003)020<1333:TRGAPSQ>2.0.CO;2)

- 431 [Liu, C., Yang, Q., Shupe, M. D., Ren, Y., Peng, S., Han, B., & Chen, D. \(2023\). Atmospheric Turbulent](#)
432 [Intermittency Over the Arctic Sea-Ice Surface During the MOSAiC Expedition. *Journal of Geophysical*](#)
433 [Research: Atmospheres, 128\(15\), e2023JD038639. <https://doi.org/10.1029/2023JD038639>](#)
- 434 [Long, M., Zhang, L., Hu, S., & Qian, S. \(2021\). Multi-Aspect Assessment of CMIP6 Models for Arctic Sea Ice](#)
435 [Simulation. *Journal of Climate, 34*\(4\), 1515–1529. <https://doi.org/10.1175/JCLI-D-20-0522.1>](#)
- 436 [López-García, V., Neely, R. R., Dahlke, S., & Brooks, I. M. \(2022\). Low-level jets over the Arctic Ocean during](#)
437 [MOSAiC. *Elementa: Science of the Anthropocene, 10*\(1\), 00063.](#)
438 <https://doi.org/10.1525/elementa.2022.00063>
- 439 [Lüpkes, C., & Grynkiv, V. M. \(2015\). A stability-dependent parametrization of transfer coefficients formomentum](#)
440 [and heat over polar sea ice to be used in climate models. *Journal of Geophysical Research: Atmospheres,*](#)
441 [120\(2\), 552–581. <https://doi.org/10.1002/2014JD022418>](#)
- 442 [Lüpkes, C., Grynkiv, V. M., Witha, B., Gryschka, M., Rassch, S., & Gollnik, T. \(2008\). Modeling convection over](#)
443 [arctic leads with LES and a non-eddy-resolving microscale model. *Journal of Geophysical Research:*](#)
444 [Oceans, 113\(9\), 1–17. <https://doi.org/10.1029/2007JC004099>](#)
- 445 [Martini, K. I., Simmons, H. L., Stoudt, C. A., & Hutchings, J. K. \(2014\). Near-inertial internal waves and sea ice in](#)
446 [the Beaufort Sea. *Journal of Physical Oceanography, 44*\(8\), 2212–2234. <https://doi.org/10.1175/JPO-D-13-0160.1>](#)
- 447 [Matrosov, S. Y., Shupe, M. D., & Uttal, T. \(2022\). High temporal resolution estimates of Arctic snowfall rates](#)
448 [emphasizing gauge and radar-based retrievals from the MOSAiC expedition. *Elementa: Science of the*](#)
449 [Anthropocene, 10\(1\), 00101. <https://doi.org/10.1525/elementa.2021.00101>](#)
- 450 [Maturilli, M., Sommer, M., Holdridge, D. J., Dahlke, S., Graeser, J., Sommerfeld, A., Jaiser, R., Deckelmann, H., &](#)
451 [Schulz, A. \(2022\). *MOSAiC radiosonde data \(level 3\)*. PANGAEA.
452 <https://doi.org/10.1594/PANGAEA.943870>](#)
- 453 [Maykut, G. A. \(1982\). Large-scale heat exchange and ice production in the central Arctic. *Journal of Geophysical*](#)
454 [Research: Oceans, 87\(C10\), 7971–7984. <https://doi.org/10.1029/JC087iC10p07971>](#)
- 455 [McNutt, S. L., & Overland, J. E. \(2003\). Spatial hierarchy in Arctic sea ice dynamics. *Tellus A: Dynamic*](#)
456 [Meteorology and Oceanography, 55\(2\), 181–191. <https://doi.org/10.3402/tellusa.v55i2.12088>](#)
- 457

- 458 [McPhee, M. G. \(2002\). Turbulent stress at the ice/ocean interface and bottom surface hydraulic roughness during the](#)
459 [SHEBA drift. *Journal of Geophysical Research*, 107\(C10\), 8037. https://doi.org/10.1029/2000JC000633](#)
- 460 [McPhee, M. G. \(2008\). *Air-Ice-Ocean Interaction: Turbulent Ocean Boundary Layer Exchange Processes* \(1st ed.\).](#)
461 [Springer. https://doi.org/10.1007/978-0-387-78335-2](#)
- 462 [McPhee, M. G., & Kantha, L. H. \(1989\). Generation of internal waves by sea ice. *Journal of Geophysical Research*,](#)
463 [94\(C3\), 3287. https://doi.org/10.1029/JC094iC03p03287](#)
- 464 [Meyer, A., Fer, I., Sundfjord, A., & Peterson, A. K. \(2017\). Mixing rates and vertical heat fluxes north of Svalbard](#)
465 [from Arctic winter to spring. *Journal of Geophysical Research: Oceans*, 122\(6\), 4569–4586.](#)
466 [https://doi.org/10.1002/2016JC012441](#)
- 467 [Meyer, A., Sundfjord, A., Fer, I., Provost, C., Villacíeros Robineau, N., Koenig, Z., Onarheim, I. H., Smedsrød, L.](#)
468 [H., Duarte, P., Dodd, P. A., Graham, R. M., Schmidtko, S., & Kauko, H. M. \(2017\). Winter to summer](#)
469 [oceanographic observations in the Arctic Ocean north of Svalbard. *Journal of Geophysical Research:*](#)
470 [Oceans, 122\(8\), 6218–6237. https://doi.org/10.1002/2016JC012391](#)
- 471 [Nansen, F. \(1902\). *The Norwegian North polar expedition, 1893–1896: Scientific Results*. London ; New York :](#)
472 [Longmans, Green and Co. ; Christiania : J. Dybwad, 1900-1906.](#)
- 473 [Nicolaus, M., Perovich, D. K., Spreen, G., Granskog, M. A., von Albedyll, L., Angelopoulos, M., Anhaus, P., Arndt,](#)
474 [S., Belter, H. J., Bessonov, V., Birnbaum, G., Brauchle, J., Calmer, R., Cardellach, E., Cheng, B., Clemens-](#)
475 [Sewall, D., Dadic, R., Damm, E., de Boer, G., ... Wendisch, M. \(2022\). Overview of the MOSAiC](#)
476 [expedition: Snow and sea ice. *Elementa: Science of the Anthropocene*, 10\(1\).](#)
477 [https://doi.org/10.1525/elementa.2021.000046](#)
- 478 [Nixdorf, U., Dethloff, K., Rex, M., Shupe, M., Sommerfeld, A., Perovich, D. K., Nicolaus, M., Heuzé, C., Rabe, B.,](#)
479 [Loose, B., Damm, E., Gradinger, R., Fong, A., Maslowski, W., Rinke, A., Kwok, R., Spreen, G.,](#)
480 [Wendisch, M., Herber, A., ... Boetius, A. \(2021\). *MOSAiC extended acknowledgement*. Zenodo.](#)
481 [https://doi.org/10.5281/zenodo.5179738](#)
- 482 [Oikkonen, A., Haapala, J., Lensu, M., Karvonen, J., & Itkin, P. \(2017\). Small-scale sea ice deformation during N-](#)
483 [ICE2015: From compact pack ice to marginal ice zone. *Journal of Geophysical Research: Oceans*, 122,](#)
484 [5105–5120.](#)

- 485 Overland, J. E. (1985). Atmospheric boundary layer structure and drag coefficients over sea ice. *Journal of*
486 *Geophysical Research: Oceans*, 90(C5), 9029–9049. <https://doi.org/10.1029/JC090iC05p09029>
- 487 Overland, J. E., & Pease, C. H. (1982). Cyclone climatology of the Bering Sea and its relation to sea ice extent.
488 *Monthly Weather Review*, 110, 5–13.
- 489 Overland, J. E., Walter, B. A., Curtin, T. B., & Turet, P. (1995). Hierarchy and sea ice mechanics: A case study from
490 the Beaufort Sea. *Journal of Geophysical Research*, 100(C3), 4559. <https://doi.org/10.1029/94JC02502>
- 491 Peng, S., Yang, Q., Shupe, M. D., Xi, X., Han, B., Chen, D., Dahlke, S., & Liu, C. (2023). The characteristics of
492 atmospheric boundary layer height over the Arctic Ocean during MOSAiC. *Atmospheric Chemistry and*
493 *Physics*, 23(15), 8683–8703. <https://doi.org/10.5194/acp-23-8683-2023>
- 494 Perovich, D., Raphael, I., Moore, R., Clemens-Sewall, D., Lei, R., Sledd, A., & Polashenski, C. (2023). Sea ice heat
495 and mass balance measurements from four autonomous buoys during the MOSAiC drift campaign.
496 *Elementa: Science of the Anthropocene*, 11(1), 00017. <https://doi.org/10.1525/elementa.2023.00017>
- 497 Persson, O., Cox, C. J., Gallagher, M. R., Shupe, M. D., Hutchings, J. K., Watkins, D. M., & Perovich, D. K. (2023).
498 *Arctic Cyclone Cloud and Boundary-Layer Features Producing Thermodynamic and Dynamic Impacts on*
499 *Arctic Sea Ice During MOSAiC*. EGU23-17554. <https://doi.org/10.5194/egusphere-egu23-17554>
- 500 Persson, P. O. G. (2002). Measurements near the Atmospheric Surface Flux Group tower at SHEBA: Near-surface
501 conditions and surface energy budget. *Journal of Geophysical Research*, 107(C10), 1–35.
502 <https://doi.org/10.1029/2000JC000705>
- 503 Persson, P. O. G. (2012). Onset and end of the summer melt season over sea ice: Thermal structure and surface
504 energy perspective from SHEBA. *Climate Dynamics*, 39, 1349–1371. [https://doi.org/10.1007/s00382-011-1196-9](https://doi.org/10.1007/s00382-011-
505 1196-9)
- 506 Persson, P. O. G., Shupe, M. D., Perovich, D., & Solomon, A. (2017). Linking atmospheric synoptic transport, cloud
507 phase, surface energy fluxes, and sea-ice growth: Observations of midwinter SHEBA conditions. *Climate*
508 *Dynamics*, 49(4), 1341–1364. <https://doi.org/10.1007/s00382-016-3383-1>
- 509 Petty, A. A., Hutchings, J. K., Richter-Menge, J. A., & Tschudi, M. A. (2016). Sea ice circulation around the
510 Beaufort Gyre: The changing role of wind forcing and the sea ice state. *Journal of Geophysical Research*,
511 19.

- 512 [Pinto, J. O., Alam, A., Maslanik, J. A., Curry, J. A., & Stone, R. S. \(2003\). Surface characteristics and atmospheric](#)
513 [footprint of springtime Arctic leads at SHEBA. *Journal of Geophysical Research: Oceans*, 108\(C4\), 8051.](#)
514 <https://doi.org/10.1029/2000JC000473>
- 515 [Rabe, B., Cox, C. C., Fang, Y.-C., Goessling, H., Granskog, M. A., Hopmann, M., Hutchings, J. K., Krumpen, T.,](#)
516 [Kuznetsov, I., Lei, R., Li, T., Maslowski, W., Nicolaus, M., Perovich, D., Persson, O., Regnery, J., Rigor,](#)
517 [I., Shupe, M. D., Sokolov, V., ... Zuo, G. \(2024\). The MOSAiC Distributed Network: Observing the](#)
518 [coupled Arctic system with multidisciplinary, coordinated platforms. *Elementa: Science of the*](#)
519 [*Anthropocene*, 12\(1\), 1–46. https://doi.org/DOI: https://doi.org/10.1525/elementa.2023.00103](#)
- 520 [Rabe, B., Heuzé, C., Regnery, J., Aksenov, Y., Allerholt, J., Athanase, M., Davies, A., Damm, E., Dethloff, K.,](#)
521 [Divine, D. V., Doglioni, F., & Craw, L. \(2022\). Overview of the MOSAiC expedition: Physical](#)
522 [oceanography. *Elementa: Science of the Anthropocene*, 10, 1–31.](#)
523 <https://doi.org/10.1525/elementa.2021.00062>
- 524 [Rae, J. G. L., Todd, A. D., Blockley, E. W., & Ridley, J. K. \(2017\). How much should we believe correlations](#)
525 [between Arctic cyclones and sea ice extent? *The Cryosphere*, 11\(6\), 3023–3034. https://doi.org/10.5194/tc-](#)
526 [11-3023-2017](#)
- 527 [Rainville, L., & Woodgate, R. A. \(2009\). Observations of internal wave generation in the seasonally ice-free Arctic.](#)
528 [*Geophysical Research Letters*, 36\(23\), L23604. https://doi.org/10.1029/2009GL041291](#)
- 529 [Richter-Menge, J. A., Perovich, D. K., & Pegau, W. S. \(2001\). Summer ice dynamics during SHEBA and its effect](#)
530 [on the ocean heat content. *Annals of Glaciology*, 33, 201–206.](#)
531 <https://doi.org/10.3189/172756401781818176>
- 532 [Rinke, A., Cassano, J. J., Cassano, E. N., Jaiser, R., & Handorf, D. \(2021\). Meteorological conditions during the](#)
533 [MOSAiC expedition. *Elementa: Science of the Anthropocene*, 9\(1\), 1–17.](#)
534 <https://doi.org/10.1525/elementa.2021.00023>
- 535 [Roberts, A., Craig, A., Maslowski, W., Osinski, R., DuVIVIER, A., Hughes, M., Nijssen, B., Cassano, J., & Brunke,](#)
536 [M. \(2015\). Simulating transient ice–ocean Ekman transport in the Regional Arctic System Model and](#)
537 [Community Earth System Model. *Annals of Glaciology*, 56\(69\), 211–228.](#)
538 <https://doi.org/10.3189/2015AoG69A760>

- 539 [Ruffieux, D., Persson, P. O. G., Fairall, C. W., & Wolfe, D. E. \(1995\). Ice pack and lead surface energy budgets](#)
540 [during LEADEX 1992. *Journal of Geophysical Research: Oceans*, 100\(C3\), 4593–4612.](#)
541 <https://doi.org/10.1029/94JC02485>
- 542 [Sandven, S., Spreen, G., Heygster, G., Girard-Ardhuin, F., Farrell, S. L., Dierking, W., & Allard, R. A. \(2023\). Sea](#)
543 [Ice Remote Sensing—Recent Developments in Methods and Climate Data Sets. *Surveys in Geophysics*.](#)
544 <https://doi.org/10.1007/s10712-023-09781-0>
- 545 [Schweiger, A. J., & Zhang, J. \(2015\). Accuracy of short-term sea ice drift forecasts using a coupled ice-ocean](#)
546 [model. *Journal of Geophysical Research: Oceans*, 15,](#)
- 547 [Selivanova, J., Iovino, D., & Cocetta, F. \(2024\). Past and future of the Arctic sea ice in High-Resolution Model](#)
548 [Intercomparison Project \(HighResMIP\) climate models. *The Cryosphere*, 18\(6\), 2739–2763.](#)
549 <https://doi.org/10.5194/tc-18-2739-2024>
- 550 [Shapiro, M. A., & Keyser, D. \(1990\). Fronts, Jet Streams and the Tropopause. In C. W. Newton & E. O. Holopainen](#)
551 [\(Eds.\), *Extratropical Cyclones* \(pp. 167–191\). American Meteorological Society.](#)
552 https://doi.org/10.1007/978-1-944970-33-8_10
- 553 [Shaw, W. J., Stanton, T. P., McPhee, M. G., Morison, J. H., & Martinson, D. G. \(2009\). Role of the upper ocean in](#)
554 [the energy budget of Arctic sea ice during SHEBA. *Journal of Geophysical Research*, 114\(C6\), C06012.](#)
555 <https://doi.org/10.1029/2008JC004991>
- 556 [Shupe, M. D., & Rex, M. \(2022\). A year in the changing Arctic sea ice. *Oceanography*, 35\(3–4\), 224–225.](#)
- 557 [Shupe, M. D., Rex, M., Blomquist, B., Persson, P. O. G., Schmale, J., Uttal, T., Buck, C., Boyer, M., Hofer, J.,](#)
558 [Hamilton, J., Posman, K., Powers, H., Pratt, K. A., Preußer, A., Rabe, B., & Rinke, A. \(2022\). Overview of](#)
559 [the MOSAiC expedition-Atmosphere. *Elementa: Science of the Anthropocene*, 10\(1\), 1–54.](#)
560 <https://doi.org/10.1525/elementa.2021.00060>
- 561 [Shupe, M. D., Rex, M., Dethloff, K., Damm, E., Fong, A. A., Gradinger, R., Heuzé, C., Loose, B., Makarov, A.,](#)
562 [Maslowski, W., Nicolaus, M., Perovich, D., Rabe, B., Rinke, A., Sokolov, V., & Sommerfeld, A. \(2020\).](#)
563 [Arctic Report Card 2020: The MOSAiC Expedition: A Year Drifting with the Arctic Sea Ice.](#)
564 <https://doi.org/10.25923/9G3V-XH92>

- 565 Stanton, T. P., & Shaw, W. J. (2023). *Observations from Autonomous Ocean Flux Buoy 46 deployed at site CO*
566 *during the MOSAiC transpolar drift, Arctic Basin, 2019-2020* [dataset]. Arctic Data Center.
567 <https://doi.org/10.18739>
- 568 Stanton, T. P., Shaw, W. J., & Hutchings, J. K. (2012). Observational study of relationships between incoming
569 radiation, open water fraction, and ocean-to-ice heat flux in the Transpolar Drift: 2002-2010: OCEAN/ICE
570 FLUXES IN THE ARCTIC. *Journal of Geophysical Research: Oceans*, 117(C7), n/a-n/a.
571 <https://doi.org/10.1029/2011JC007871>
- 572 Taylor, K. E., Stouffer, R. J., & Meehl, G. a. (2012). An overview of CMIP5 and the experiment design. *Bulletin of*
573 *the American Meteorological Society*, 93(4), 485–498. <https://doi.org/10.1175/BAMS-D-11-00094.1>
- 574 Taylor, P. C., Hegyi, B. M., Boeke, R. C., & Boisvert, L. N. (2018). On the increasing importance of air-sea
575 exchanges in a thawing Arctic: A review. *Atmosphere*, 9(2), 1–39. <https://doi.org/10.3390/atmos9020041>
- 576 Thorndike, A. S. (1986). Diffusion of sea ice. *Journal of Geophysical Research*, 91(C6), 7691.
577 <https://doi.org/10.1029/JC091iC06p07691>
- 578 Thorndike, A. S., & Colony, R. (1982). Sea ice motion in response to geostrophic winds. *Journal of Geophysical*
579 *Research*, 87(C8), 5845. <https://doi.org/10.1029/JC087iC08p05845>
- 580 Toole, J., Krishfield, R., Timmermans, M.-L., & Proshutinsky, A. (2011). The Ice-Tethered Profiler: Argo of the
581 Arctic. *Oceanography*, 24(3), 126–135. <https://doi.org/10.5670/oceanog.2011.64>
- 582 Toole, J. M., Timmermans, M. -L., Perovich, D. K., Krishfield, R. A., Proshutinsky, A., & Richter-Menge, J. A.
583 (2010). Influences of the ocean surface mixed layer and thermohaline stratification on Arctic Sea ice in the
584 central Canada Basin. *Journal of Geophysical Research: Oceans*, 115(C10), 2009JC005660.
585 <https://doi.org/10.1029/2009JC005660>
- 586 Uttal, T., Curry, J. A., McPhee, M. G., Perovich, D. K., Moritz, R. E., Maslanik, J. A., Guest, P. S., Stern, H. L.,
587 Moore, J. A., Turenne, R., Heiberg, A., Serreze, M. C., Wylie, D. P., Persson, O. G., Paulson, C. A., Halle,
588 C., Marison, J. H., Wheeler, P. A., Makshtas, A., ... Grenfeld, T. C. (2002). Surface heat budget of the
589 arctic ocean. *Bulletin of the American Meteorological Society*, 83(2), 255–275.
590 [https://doi.org/10.1175/1520-0477\(2002\)083<0255:SHBOTA>2.3.CO;2](https://doi.org/10.1175/1520-0477(2002)083<0255:SHBOTA>2.3.CO;2)

- 591 [Ustinoka, M., Polojärvi, A., & Haapala, J. \(2024\). Local-scale analysis on sea-ice deformation based on radar](#)
592 [imagery and deep learning. EGU24-19034. EGU General Assembly 2024, Vienna, Austria.](#)
593 <https://doi.org/10.5194/egusphere-egu24-19034>
- 594 [Vessey, A. F., Hodges, K. I., Shaffrey, L. C., & Day, J. J. \(2020\). An inter-comparison of Arctic synoptic scale](#)
595 [storms between four global reanalysis datasets. *Climate Dynamics*, 2777–2795.](#)
- 596 [Vessey, A. F., Hodges, K. I., Shaffrey, L. C., & Day, J. J. \(2022\). The composite development and structure of](#)
597 [intense synoptic-scale Arctic cyclones. *Weather and Climate Dynamics*, 3\(3\), 1097–1112.](#)
598 <https://doi.org/10.5194/wcd-3-1097-2022>
- 599 [von Albedyll, L., Hendricks, S., Grodofzig, R., Krumpen, T., Arndt, S., Belter, H. J., Birnbaum, G., Cheng, B.,](#)
600 [Hoppmann, M., Hutchings, J., Itkin, P., Lei, R., Nicolaus, M., Ricker, R., Rohde, J., Suhrhoff, M.,](#)
601 [Timofeeva, A., Watkins, D., Webster, M., & Haas, C. \(2022\). Thermodynamic and dynamic contributions](#)
602 [to seasonal Arctic sea ice thickness distributions from airborne observations. *Elementa: Science of the*](#)
603 [Anthropocene](#), 10(1), 00074. <https://doi.org/10.1525/elementa.2021.00074>
- 604 [Wang, C., Graham, R. M., Wang, K., Gerland, S., & Granskog, M. A. \(2019\). Comparison of ERA5 and ERA-](#)
605 [Interim near-surface air temperature, snowfall and precipitation over Arctic sea ice: Effects on sea ice](#)
606 [thermodynamics and evolution. *The Cryosphere*, 13\(6\), 1661–1679. <https://doi.org/10.5194/tc-13-1661-2019>](#)
- 607 [Wang, X., Chen, R., Li, C., Chen, Z., Hui, F., & Cheng, X. \(2022\). An Intercomparison of Satellite Derived Arctic](#)
608 [Sea Ice Motion Products. *Remote Sensing*, 14\(5\), 1261. <https://doi.org/10.3390/rs14051261>](#)
- 609 [Watkins, D. M., Bliss, A. C., Hutchings, J. K., & Wilhelmus, M. M. \(2023\). Evidence of Abrupt Transitions](#)
610 [Between Sea Ice Dynamical Regimes in the East Greenland Marginal Ice Zone. *Geophysical Research*](#)
611 [Letters](#), 50(e2023GL103558), 1–10.
- 612 [Webster, M. A., Parker, C., Boisvert, L., & Kwok, R. \(2019\). The role of cyclone activity in snow accumulation on](#)
613 [Arctic sea ice. *Nature Communications*, 10\(1\), 5285. <https://doi.org/10.1038/s41467-019-13299-8>](#)
- 614 [Weiss, J., & Dansereau, V. \(2017\). Linking scales in sea ice mechanics. *Philosophical Transactions of the Royal*](#)
615 [Society A: Mathematical, Physical and Engineering Sciences](#), 375(20150352), 1–17.
616 <https://doi.org/10.1098/rsta.2015.0352>
- 617

- 618 [Womack, A., Vichi, M., Alberello, A., & Toffoli, A. \(2022\). Atmospheric drivers of a winter-to-spring Lagrangian](#)
619 [sea-ice drift in the Eastern Antarctic marginal ice zone. *Journal of Glaciology*.](#)
620 <https://doi.org/10.1017/jog.2022.14>
- 621 [Yang, J. \(2004\). Storm-driven mixing and potential impact on the Arctic Ocean. *Journal of Geophysical Research*,](#)
622 [109\(C4\), C04008. https://doi.org/10.1029/2001JC001248](#)
- 623 [Yu, Y., Xiao, W., Zhang, Z., Cheng, X., Hui, F., & Zhao, J. \(2021\). Evaluation of 2-m Air Temperature and Surface](#)
624 [Temperature from ERA5 and ERA-I Using Buoy Observations in the Arctic during 2010–2020. *Remote*](#)
625 [Sensing, 13\(14\), 2813. https://doi.org/10.3390/rs13142813](#)
- 626 [Yuan, D., Hao, Z., You, J., Zhang, P., Yin, B., Li, Q., & Xu, Z. \(2022\). Enhancing Sea Ice Inertial Oscillations in the](#)
627 [Arctic Ocean between 1979 and 2019. *Water*, 15\(1\), 152. https://doi.org/10.3390/w15010152](#)